AN EFFECTIVE NOTCH STRESS CONCEPT BASED TOTAL FATIGUE LIFE ESTIMATE OF MARITIME STRUCTURES

XINMIAO LIU

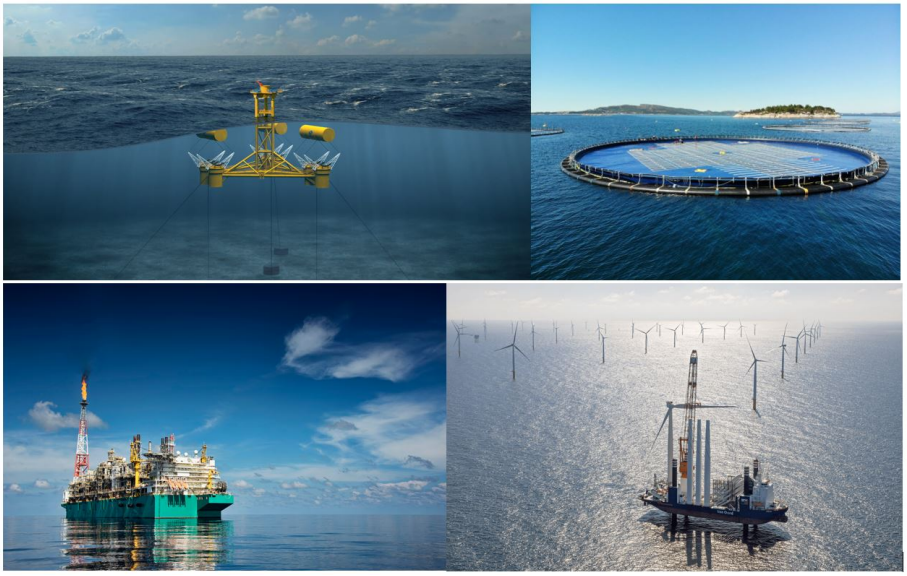

Maritime and Transport Technology
Mechanical, Maritime and Materials Engineering
Delft University of Technology

November 2022

SUPERVISOR(S):
Dr.ir. J. H. den Besten
Ir. Bas Aberkrom
Ir. Gabriele Bufalari

LOCATION:
Delft, Zuid-Holland, the Netherlands

TIME FRAME:
November 2021 – November 2022

Thesis for the degree of MSc in Marine Technology in the specialization of Ship and Offshore Structures

AN EFFECTIVE NOTCH STRESS CONCEPT BASED TOTAL FATIGUE LIFE ESTIMATE OF MARITIME STRUCTURES

By

XINMIAO LIU

Performed at

FEMTO ENGINEERING

This thesis (MT.22/23.015.M) is classified as confidential in accordance with the general conditions for projects performed by the TUDelft. Monday November 11, 2022 at 15:00 (CEST).

Student number:	5217938	
Thesis committee:	Dr.ir. J. H. den Besten,	TU Delft, chair
	Ir. Wouter van den Bos ,	TU Delft, member
	Ir. Gabriele Bufalari,	TU Delft, supervisor
	Ir. Bas Aberkrom,	FEMTO, supervisor

This page intentionally left blank

ABSTRACT

Fatigue is typically a governing limit state for maritime structures, and weld joints are the most critical locations. Various fatigue damage criteria have been developed involving either an intact or cracked geometry parameter, incorporating local or global information. In this thesis, the effective notch stress based total life fatigue damage criterion has been used in order to improve the accuracy of fatigue lifetime prediction and reduce the workload of engineers in the early design stage. First, the Battelle structural stress calculation procedure is clarified and examined with three models. A hot spot type A, B and C mesh convergence study are conducted. In order to quantify the influence of mesh quality, several ugly mesh models are tested with their good mesh counterparts. For validation purposes of the total life model, a large scale specimen fatigue test result has been used and the mesh quality investigations are included. The DNV-GL based life time estimate is provided for the sake of comparison. Finally, several conclusions and recommendations are provided for future applications.

KEYWORDS — Fatigue design, joint resistance curve, steel marine structures, total life concept, structural stress, welded joints.

This page intentionally left blank

CONTENTS

LIST OF FIGURES

LIST OF TABLES

This page intentionally left blank

ACRONYMS

CTSEDC	crack tip strain energy density concept
ENSC	effective notch stress concept
FEM	finite element method
GRFL	generalised random fatigue limit
GVNM	generalized virtual node method
HCF	high cycle fatigue
HS	hot spot
HSSS	hot spot structural stress
HSSSC	hot spot structural stress concept
LC	load carrying
LB	linaer Basquin
LDM	linear damage model
LSS	large scale specimen
MCF	mid cycle fatigue
NLC	non-load carrying
NSC	nominal stress concept
NSIFC	notch stress intensity factor concept
ORFL	ordinary random fatigue limit
SIF	stress intensity factor
SSS	small scale specimen
TCD	Theory of Critical Distances
TSC	total stress concept
VA	variable amplitude

NOMENCLATURE

Latin symbols

A	material constants for critical distance factor
B	material constants as critical distance exponential
C_{bw}	weld load carrying stress coefficient
D	(total) fatigue damage
E	bulk modulus of elasticity
F_a	nodal force corresponds to nodes in index a
F_i	nodal force at node i
F_c	nodal force corresponds to nodes in index c
G	shear modulus
I_N	notch crack growth integral
K	stress intensity factor
K'	cyclic strength coefficient
K_f	notch factor
K_I	mode-I stress intensity factor
N	(total) number of cycles until failure (i.e. through-thickness crack)
N_g	number of cycles corresponding to crack growth
N_i	number of cycles corresponding to crack initiation
S	stress range / stress structural response parameter
S_e	effective (notch) stress range
S_h	hot spot structural stress range
S_n	nominal stress range
S_T	total stress range

S_{inf}	fatigue limit
Y_f	far field factor
Y_{fb}	far field factor bending component
Y_{fm}	far field factor membrane component
Y_{fw}	weld reinforcement affected far field factor
Y_n	notch factor
a/a_c	crack size
a_0	critical crack size
a_f	final crack size / fictitious crack size
a_i	(real) defect- or initial crack size
a_k	line force gradient within kth element
a_n	(root) notch size
a_t	crack transition size
b	cyclic fatigue strength exponent
b_k	line force intercept within kth element
c	set of nodes 1 to n-1 within the crack length
$\bar{f}$	linearized line force over l
f_i	line force at finite element i
f_m	line membrane force
f_y	line membrane force in local y-direction
f_z	line membrane force in local z-direction
k	notch stress intensity weight function
k_1	mode-I notch stress intensity weight function
k_2	mode-II notch stress intensity weight function
l	reference length
l_1	crack length
l_w	weld leg length
l_i	ith element edge length
h_w	weld leg height

$\bar{m}$	l_1 linearization slope
m_1	fatigue resistance HCF slope
m_2	fatigue resistance MCF slope
m_b	line bending moment
n	number of cycles/notch elasto-plasticity coefficient
r_s	structural bending stress ratio
s	curvilinear abscissa
t_p	plate thickness
t_b	base plate thickness
t_c	connecting, cross, cover plate thickness
$\bar{u}$	virtual displacement

Greek symbols

ΔK_I	mode-I crack growth driving force
$\Delta\sigma_0$	fatigue limit of structures
$\Delta\sigma_s$	structural stress range
α	(half) notch angle
β	stress angle
γ	load ratio coefficient/welded joint cross plate angle
δ	data type {complete = 1, censored = 0}
ϵ_e	elastic strain component
ϵ'_f	cyclic fatigue strain coefficient
ϵ_p	plastic strain component
λ	eigenvalue
λ_i	eigenvalue (asymptotic solution)
$\{\lambda_a, \lambda_s\}$	first eigenvalue of (anti-)symmetry part
μ	mean value
$\{\mu_a, \mu_s\}$	stress amplitude of (anti-)symmetry part
ν	Poisson ratio
ρ	real notch radius

ρ_c	critical dislocation density
ρ_e	effective notch radius
ρ_f	fictitious notch radius
ρ^*	micro-structural support length
σ	stress/standard deviation
σ_a	stress amplitude
σ_b	bending stress component
σ_f	structural, welded joint far field stress distribution
σ'_f	cyclic fatigue strength coefficient
σ_h	hot spot stress (amplitude)
σ_{l_0}	fatigue limit for fully reversed conditions
σ_m	mean stress/structural membrane stress component
σ_{max}	peak stress
σ_n	nominal stress (amplitude) / weld toe notch stress distribution
σ_s	structural stress (amplitude)
σ_{se}	self-equilibrating stress part
σ_u	ultimate tensile strength
σ_y	material yield stress / strength
$\{\chi_a, \chi_s\}$	first eigenvalue coefficient of (anti-)symmetry part
χ_i	eigenvalue coefficient of asymptotic solution

This page intentionally left blank

1

INTRODUCTION

1.1 MOTIVATION

Sustainable maritime structures like wind turbines are subject to cyclic mechanical loads, not only induced by environments like waves and wind, but also by internal machinery(Sadananda & Vasudevan, 2003). Fatigue is a significant limit state for the lifetime of the maritime structure, and weld notches are the governing positions. Design assessment guidelines, recommendations, and codes like NEN2063 and DNV-GL are widely used in the maritime industry. However, the accuracy of the prediction is not satisfactory. The nominal stress concept (NSC) and hot spot structural stress concept (HSSSC) are the most widely used, but results are sensitive to mesh quality and mesh size, which requires engineering judgment on geometry details to some extent.

According to Dong (2005), a mesh insensitive Battelle structural stress approach is developed to determine the structural stress level at the weld notch location(figure 1.1 and 1.2). The modeling workload would be largely reduced during the early design stage if the method is implemented correctly. However, there is hardly any information available quantifying the mesh insensitivity of Battelle structural stress, nor clarifying the method procedure.

In addition, fatigue life time prediction accuracy can be improved by using a total life estimate. A one-parameter two-stage effective

notch stress based total life estimate seems to have a good balance between accuracy and simplicity(H. den Besten, 2018).

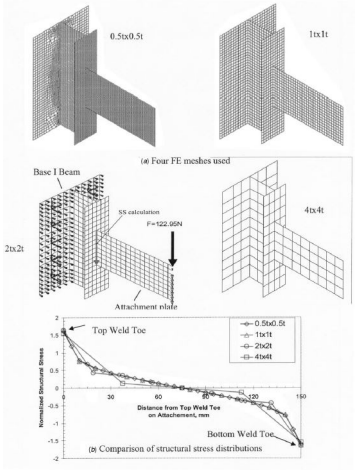

Figure 1.1: Mesh-size insensitivity demonstration for an edge detail investigated(Dong, 2005) for hot spot type B and C

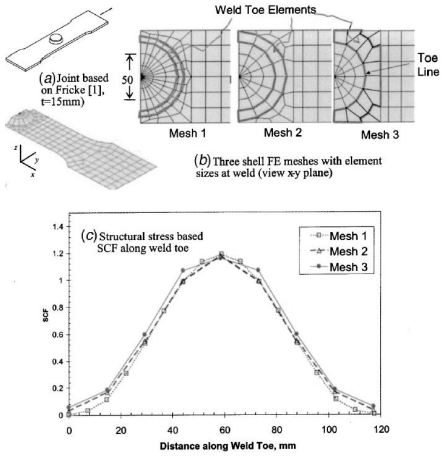

Figure 1.2: Mesh-size insensitivity demonstration for an edge detail investigated(Dong, 2005) for C

1.1.1 *Fatigue Damage Criteria*

Various criteria are available to analyze fatigue damage of structures based on different parameters. Generally, the fatigue damage criterion can be sorted into the following classifications in figure 1.3(J. H. den Besten, 2015):

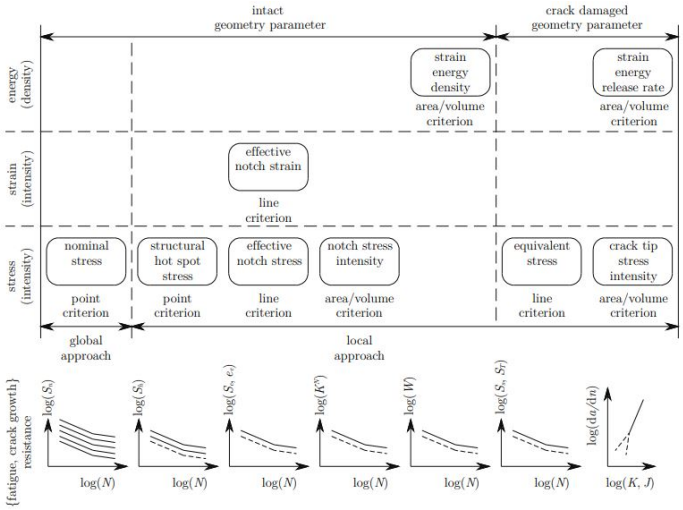

Figure 1.3: Fatigue assessment concept overview

In this section, NSC, HSSSC, effective notch stress concept (ENSC), notch stress intensity factor concept (NSIFC), crack tip strain energy density concept (CTSEDC) and total stress concept (TSC) would be discussed.

1.1.1.1 *Nominal Stress*

Nominal stress concept is a global intact geometry parameter-based point criterion. For a simple structure under mid cycle fatigue (MCF) and high cycle fatigue (HCF), the nominal stress concept is often used to evaluate the fatigue damage. As shown in figure 1.4, nominal

stress for a cruciform joint σ_n is assumed to be constant along the plate thickness.

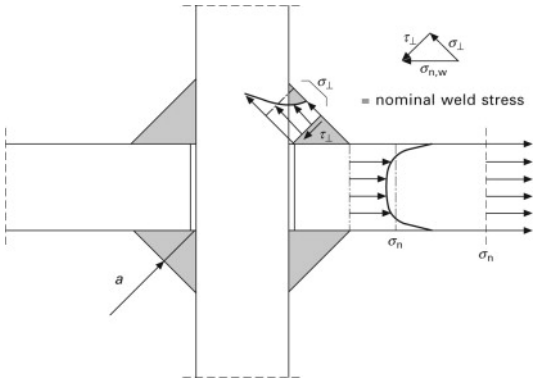

Figure 1.4: Nominal stress

The nominal stress range $S_n = \Delta\sigma_n$ is either obtained by hand calculations or output from FEM models. Once the material, geometry details, loading & response, environment, failure location and weld quality information are available, further calculation effort is limited. The stress concentration factor has already been available for different structural details and load conditions based on small scale specimen (SSS) and large scale specimen (LSS) experiments.

1.1.1.2 *Hot Spot Structural Stress*

The hot spot structural stress concept is an intact geometry parameter local point criterion. The hot spot structural stress is defined as the equilibrium equivalent stress at the hot spot location in the cross-section of the crack path. Self-equilibrating stress influence induced by t_b, t_c,l_w, h_w, etc. are not considered in the calculation, which illustrated that still infinite number of S-N curve exist. Most widely used method to calculate hot spot structural stress (HSSS) is linear surface extrapolation. The structural stress at the notch location is calculated by extrapolating with two reference points near the hot spot. Once the hot spot structural stress is developed, it is easy

to determine the fatigue lifetime through the S-N curve. The load carrying (LC) and non-load carrying (NLC) details should differentiate with two fatigue resistance curve, and the identification sometimes requires engineering judgement.

1.1.1.3 *Effective Notch Stress*

To overcome the weakness of hot spot structural stress, the ENSC was developed as an intact geometry parameter based local line criterion. It came from the Theory of Critical Distances (TCD), which is proposed by Neuber (1961). As shown in figure 1.5, the notch stress is the non-linear stress distribution through the plate thickness at the hot spot, which can be related to structural stress and weld dimensions(J. H. den Besten, 2015).

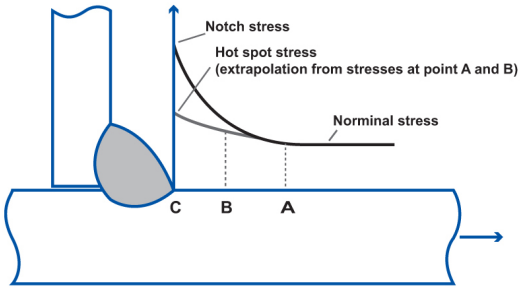

Figure 1.5: Fatigue structural stress and notch stress

The effective notch stress concept is based on the averaged notch stress value over a material characteristic length ρ^* below the plate surface. The ρ^* represents the distance where the majority of the life time is consumed. The analytical solution of notch stress distribution has been available(J. H. den Besten, 2015) and the calculation procedure of ρ^* becomes the key question. It is most likely to be obtained using regression analysis and an iterative approach. Once the effective notch stress has been determined, there is no need for engineering judgment because only one S-N curve is required. Moreover, throughout the approach to effective notch stress, the geometry,

notch stress gradient, and loading & response contribution are taken into account, enabling the prediction more accurate than hot spot structural stress concept.

1.1.1.4 *Crack Tip Stress Intensity*

The crack tip stress intensity $K(\sigma, a)$ is a cracked geometry criterion. In this model, fatigue damage of arc-welded marine structures is supposed to be a process dominated by crack propagation. Hence, the linear elastic stress and crack size effect determined stress intensity factor is employed to evaluate the life span(Paris, 2014). For crack at weld toe notch, SIF can be expressed by a weight function method(Glinka & Shen, 1991):

$$K = \sigma \cdot Y_n(a) \cdot Y_f(a) \cdot \sqrt{\pi a} \tag{1.1}$$

The cyclic loading $K(\sigma, a)$ becomes a crack driving force $\Delta K(\Delta\sigma, a)$. To achieve crack growth, the applied SIF value should either exceed the maximum threshold value ($K_{max,appl} > K_{max,th}$) or the applied SIF range should be larger than the threshold value $\Delta K_{appl} > \Delta K_{th}$. Usually, the ΔK_{th} is always small and will be reached first in practical cases(H. den Besten, 2018).

Paris' equation can express the fatigue crack growth rate with the two-parameter crack driving force(Noroozi *et al.*, 2005):

$$\frac{\mathrm{d}a}{\mathrm{d}N} = C \cdot \left[K_{tot,max}^{p} \Delta K_{tot}^{1-p}\right]^{\gamma} \tag{1.2}$$

By integrating eq. 1.2, the fatigue lifetime for the propagation phase can be identified. The advantage of this method is that it only requires a single fatigue resistance curve, and factors such as size effect and residual stress component can be incorporated via stress intensity factor (SIF). However, because the model disregards the fatigue initiation contribution, it is not very accurate for mid-to-high cycle fatigue.

1.1.1.5 *Total Stress*

The total stress concept is a cracked geometry and stress intensity based area equivalent line criterion proposed by J. H. den Besten (2015). It aims to improve fatigue strength similarity with respect to weld notch stress intensity, far-field dominated macro-crack growth, welded joint fatigue resistance similarity etc. The total stress parameter is introduced by J. H. den Besten (2015) to determine the fatigue life time:

$$S_T = \frac{\Delta\sigma_s}{(1-\eta_r)^{1-\gamma} \cdot I_N^{\frac{1}{m}} \cdot t_p^{\frac{2-m}{2m}}} \tag{1.3}$$

with the notch integral I_N

$$I_N = \int_{\frac{a_i}{t_p}}^{\frac{a_f}{t_p}} \frac{1}{\left\{Y_n\left(\frac{a}{t_p}\right)\right\}^n \cdot \left\{Y_f\left(\frac{a}{t_p}\right)\right\}^m \cdot \left(\frac{a}{t_p}\right)^{\frac{m}{2}}} \, \mathrm{d}\left(\frac{a}{t_p}\right) \tag{1.4}$$

For decreasing S_T, the micro-crack growth behavior is transformed from elasto-plastic into elastic. A way to solve this problem is using a random fatigue limit estimate by estimating the MCF n value and applying an elasto-plasticity induced HCF correction. The generalised random fatigue limit (GRFL) form non-linear S-N curve can be expressed as:

$$\log(N) = \log(C) - m \cdot \log(S_T) - \rho_{S\infty} \cdot \log\left\{1 - \frac{S_\infty(\mu,\sigma)}{S_T}\right\} \tag{1.5}$$

The total stress concept improved the fatigue strength similarity behavior through the total stress parameter. The gradient induced size effect is explicitly taken into account. However, the notch integral I_N computation requires much more effort than traditional method, so it is difficult to implement.

1.1.2 *Total life Concept*

In the past, the total life of the structure was separated into crack initiation(Ramberg-Osgood relation) and crack growth(through stress

intensity factor) lifetime(Darcis *et al.*, 2006). Each period is calculated with different method and finally added up through linear superposition. However, it is very difficult to identify the transition crack length between initiation and growth, making the lifetime estimation rather erroneous. In this instance, a two-stage, one-parameter model is demonstrated.

1.1.2.1 *Effective Notch Stress*

According to the effective notch stress concept, ρ^* is defined as a constant material property-dependent parameter. It is pretty accurate for mid-to-high cycle fatigue calculation but will underestimate the MCF load case. However, if ρ^* becomes load level dependent, effective notch stress concept can be used to predict both initiation and growth lifetime. ρ^* is small in HCF range, as most of the lifetime is consumed at material surface. As external load increases, ρ^* would become larger since crack growth dominates the lifetime, compensating for the underestimation of original approach.

Theory of Critical Distance Based on SIF

A method based on Theory of Critical Distances can be adopted to calculate ρ^* as the load level dependent material parameter. It is assumed that the effective notch stress is equal to the stress at a fictitious point away from the notch. Moreover, the fatigue limit $\Delta\sigma_0$ can be related to threshold SIF and crack length(Taylor, 1999):

$$\Delta\sigma_0 = \frac{\Delta K_{th}}{(a_c)^{\frac{1}{2}}} \tag{1.6}$$

The stress range dependent critical distance may be expressed as:

$$a_{0,M} = \left(\frac{1}{\pi}\right)\left(\frac{\Delta K}{\Delta\sigma_{ref}}\right)^2 \tag{1.7}$$

σ_{ref} is the reference stress range for each load case.

Theory of Critical Distance Based on Failure Life Time

According to Susmel and Taylor (2007) study, an alternative critical distance for MCF range based on failure life time can be rewritten as:

$$a_{0,M}(N_f) = AN_f^B \tag{1.8}$$

Material constants A and B in eq. 1.8, where $A > 0$ and $B < 0$, are carried out by regression analysis and iterative approach. Stress concentration factor K_t can be introduced due to the size effect contribution(Yang *et al.*, 2011):

$$a_{0,M} = K_t^m \cdot AN_f^B \tag{1.9}$$

Material Characteristic Length Based on Structural Stress

Experimental data shows exponential relation between ρ^* and stress level. If the failure life time in eq. 1.8 is substituted by effective notch stress range S_e, it is possible to using iterative approach and regression analysis to carry out a equation of ρ^* and stress range accordingly. Therefore, Palkar(2021) has developed a method to estimate ρ^* with structural stress range, yield strength and load ratio:

$$\rho^* = \rho_c \left(\frac{\Delta\sigma_s / (1 - r_{lr})}{\sigma_y} \right)^{\rho_p^*} \tag{1.10}$$

where ρ_c and ρ_p^* are material fitting constants. According to the standard deviation of maximum likelihood estimation, the best fit happens at $\rho_c = 2.04$ and $\rho_p^* = 1$.

1.1.2.2 *Total Stress*

The total stress concept is a cracked geometry based criterion suitable for calculating the fatigue lifetime of a crack propagation-dominated load case. The assumption can be made that one of the parameters within the total stress S_T is load level dependent and thus applicable for the crack initiation stage.

For calculating total stress, the notch crack growth integral I_N uses the initial crack length as the lower bound and the final crack length

as the upper bound. Both parameters are constants for a particular load condition and structural detail. It is feasible to make the initial crack length and the final crack length dependant on the load level. On the other hand, the elasto-plasticity coefficient n was derived from the well-known Ramberg-Osgood relation, where $n = 1$ for linearly elastic material and n=infinity for completely elastic material. Consequently, the elasto-plasticity coefficient n could also assumed to be a load-dependent parameter.

1.1.3 *Research Objectives*

It is vital to perform accurate stress assessments to ensure that the structure is durable enough to prevent failure throughout its lifetime. Using the one-parameter two-stage model, this study seeks to build and investigate a more precise method for predicting the lifetime of welded structures. Implement and verify a precise and mesh-insensitive Battelle structural stress method. The load level dependent total life model would be validated with experimental results to examine its accuracy.

1.2 THESIS OUTLINE

The thesis will employ an effective notch stress based total life estimate method to predict the fatigue lifetime of structures. First, a weld(fatigue sensitive location) recognition algorithm will be developed to output necessary data such as nodal forces and geometry details from a FEM model. Chapter 2 would next apply and test the Battelle structural stress. As verification, several different mesh size and mesh quality models will be compared. In the next stage, the effective notch stress procedure is applied to predict the total life span of structures. In Chapter 4, a large scale specimen test results will be presented as validation purpose. Finally, the discussion and conclusion of the whole project would be given. Recommendations were provided for future study convenience.

2

FAR FIELD STRESS CALCULATION

The far field stress is of great importance for estimating the stress at the weld location. Nowadays, nominal stress and hot spot structural stress have been widely employed in the industry due to its simplicity. However, both of the method has its own limitations. Hot spot structural stress is sensitive to mesh size and nominal stress is difficult to capture in complex structures. On the other hand, both methods are more or less dependent on engineering judgement, which causes inaccurancy in some extent. In this chapter, the Battelle structural stress method would be clarified.

2.1 INPUT PARAMETERS

Initially, it is necessary to summarize the input parameters that are necessary for stress computation, which include geometry input and structural response input. The geometry input can be separated into two groups: structure dimensions and structure details. To determine the linear/non-linear through-thickness stress distribution, it is important to know the parameters of the structure's plate thickness and weld geometry. In order to convert structural reaction (nodal forces/-moments) into stress, it is also necessary to know the dimensions of other FEM output, such as the node coordinates along the weld. In addition, normal vectors of the elements are required to establish the local coordinate system.

Structural details contains information like weld joints types(T joint or cruciform joint) and hot spot types(hot spot A, B and C). The through-thickness linearized stress component(structural stress) and actual non-linear notch stress distribution should be calculated for each type separately.

To determine Battelle structural stress, nodal forces and moments are output as structural response. All the parameters are summarized in the table 2.1:

Table 2.1: Input Parameter

Geometry detail	**Structural Response**
Joint Type	Nodal Forces
Hot Spot Type	Nodal Moments
Plate Thickness	
Weld Height	
Weld length	
Node Coordinates	
Element Center Coordinates	
Element Normal Vector	

2.2 THROUGH-THICKNESS LINEARIZATION OF BETTELLE STRUCTURAL STRESS

For linear shell model static analysis, the following equation must be satisfied(Dong, 2005):

$$\{F\} = [K]\{U\} \tag{2.1}$$

where $[K]$ is the global stiffness matrix with dimension $N \times N$, $[U]$ is the vector of displacements and rotations with N elements, $[F]$ is the vector of nodal forces and nodal moments, and N is the number of degrees of freedom of the system. Vector $[U]$ contains the displacements and rotations of all nodes in the global coordinate system.

Therefore, the global stiffness matrix is formed by appropriately assembling the stiffness matrices of each element $[K_e]$. After solving Eq. 2.1, the vector containing the element nodal forces and nodal moments acting on each node of the individual element on the weld line. The element nodal force vector, can be computed as follows:

$$\{F_e\} = [K_e]\{U\} \tag{2.2}$$

The element nodal forces in the local coordinate system (x', y', z') can then be computed as:

$$\left\{\mathrm{F}^{e\prime}\right\} = [\mathbf{T}]\left\{\mathrm{F}^{e}\right\} \tag{2.3}$$

where $\{\mathrm{F}^{e\prime}\}$ is the vector carrying the nodal forces and nodal moments acting in the specific element in the local coordinate system and $[\mathbf{T}]$ is the appropriate rotation matrix made up of sines and cosines of the angles between the global and local coordinate systems. For computation simplicity, the rotation matrix for every element can be computed by the the global coordinate systems and local coordinate systems:

$$[R] = \begin{bmatrix} x \\ y \\ z \end{bmatrix}^{-1} \cdot \begin{bmatrix} x' \\ y' \\ z' \end{bmatrix} \tag{2.4}$$

The calculation of structural stresses is carried out by a procedure known as structural stress recovery, in which the local coordinate system's nodal forces (F_i along the $y\prime$-axis and nodal moments (M_i about the $x\prime$-axis) are first translated into line forces (f_i) and line moments (m_i) acting on the weld path. One may determine the local equilibrium of forces and moments at a single element from(Alencar *et al.*, 2021):

$$\sum F_{y'i} + \int_0^l f_{y'}(x)\mathrm{d}x = 0 \tag{2.5}$$

$$\sum F_{y'i}x_i + \int_0^l f_{y'}(x)x\mathrm{d}x = 0 \tag{2.6}$$

$$\sum M_{x'i} + \int_0^l m_{x'}(x)\mathrm{d}x = 0 \tag{2.7}$$

$$\sum M_{x'i'} x_i + \int_0^l m_{x'}(x)x\mathrm{d}x = 0 \tag{2.8}$$

For a 4-noded shell element with an edge over the weld line, the equilibrium line forces Eq. 2.5-2.8 yields to:

$$f_1 = \frac{2}{l}(2F_1 - F_2) \tag{2.9}$$

$$f_2 = \frac{2}{l}(2F_2 - F_1) \tag{2.10}$$

$$m_1 = \frac{2}{l}(2M_1 - M_2) \tag{2.11}$$

$$m_2 = \frac{2}{l}(2M_2 - M_1) \tag{2.12}$$

The nodal forces and nodal moments can be rewritten as:

$$F_1 = \frac{l}{6}(2f_1 + f_2) \tag{2.13}$$

$$F_2 = \frac{l}{6}(2f_2 + f_1) \tag{2.14}$$

$$M_1 = \frac{l}{6}(2m_1 + m_2) \tag{2.15}$$

$$M_2 = \frac{l}{6}(2m_2 + m_1) \tag{2.16}$$

In order to model the stress vector distribution on the weld line, the forces and moments should be continuous except on material boundaries on the plate surface. It results from the assumed continuity of the stress solution along the weld geometry. This may not be the case at end points where weld line geometry is discontinuously differentiable, at jumps in applied surface forces, or at jumps in material properties. In this project, the discontinuity effect of the weld is not considered.

The influence of adjacent elements must be considered for equilibrium when calculating the structural stresses for a series of elements on the weld line. Eqs. 2.13 to 2.16 change because it is likely that there is a line force or moment discontinuity across the boundary:

$$F_1 = \frac{l}{6}\left(2f_1 + f_2^L\right) \tag{2.17}$$

$$F_2^L = \frac{l}{6}\left(2f_2^L + f_1\right) \tag{2.18}$$

$$F_2^R = \frac{l_2}{6}\left(2f_2^R + f_3\right) \tag{2.19}$$

$$F_3 = \frac{l_2}{6}\left(2f_3 + f_2^R\right) \tag{2.20}$$

The same equations can be obtained for nodal moments. In order to overcome the discontinuity, a simple approach(Kim *et al.*, 2010) is used by assuming $f_2^L = f_2^R = f_2$ at the mutual node. Then, the line forces of the first three node along the weld line becomes:

$$F_1 = \frac{l_1}{3}f_1 + \frac{l_1}{6}f_2 \tag{2.21}$$

$$\begin{aligned} F_2 &= F_2^L + F_2^R = \frac{l_1}{6}\left(2f_2^L + f_1\right) + \frac{l_2}{6}\left(2f_2^R + f_3\right) \\ &= \frac{l_1}{6}f_1 + \frac{(l_1 + l_2)}{3}f_2 + \frac{l_2}{6}f_3 \end{aligned} \tag{2.22}$$

$$F_3 = \frac{l_2}{6} f_2 + \frac{l_2}{3} f_3 \tag{2.23}$$

For n-elements in the row, the following formulae are proposed in a more general form:

$$F_i = \frac{l_{i-1}}{6} f_{i-1} + \frac{(l_{i-1} + l_i)}{3} f_i + \frac{l_i}{6} f_{i+1} \tag{2.24}$$

$$F_{i+1} = \frac{l_i}{6} f_i + \frac{(l_i + l_{i+1})}{3} f_{i+1} + \frac{l_{i+1}}{6} f_{i+2} \tag{2.25}$$

$$F_{i+2} = \frac{l_{i+1}}{6} f_{i+1} + \frac{(l_{i+1} + l_{i+2})}{3} f_{i+2} + \frac{l_{i+2}}{6} f_{i+3} \tag{2.26}$$

Furthermore, for a closed weld path, where the last node coinciding with the first one, Eqs. 2.24 to 2.26 can be expressed in the following matrix form:

$$\begin{Bmatrix} F_1 \\ F_2 \\ \vdots \\ F_{n-1} \\ F_n \end{Bmatrix} = \begin{bmatrix} \frac{l_1}{3} & \frac{l_1}{6} & 0 & 0 & \dots & 0 \\ \frac{l_1}{6} & \frac{l_1+l_2}{3} & \frac{l_2}{6} & 0 & \dots & \vdots \\ 0 & \frac{l_2}{6} & \frac{l_2+l_3}{3} & \frac{l_3}{6} & & \\ \vdots & & & \ddots & \frac{l_{n-2}+l_{n-1}}{3} & \frac{l_{n-1}}{6} \\ 0 & \dots & & 0 & \frac{l_{n-1}}{6} & \frac{l_{n-1}}{3} \end{bmatrix} \begin{Bmatrix} f_1 \\ f_2 \\ \vdots \\ f_{n-1} \\ f_n \end{Bmatrix} \tag{2.27}$$

The structural stress can be expressed as a superposition of membrane stress and bending stress:

$$\sigma_s = \sigma_m + \sigma_b = f_n / t_p + 6 \cdot m_b / t_p^2 \tag{2.28}$$

2.3 GENERALIZED VIRTUAL NODE METHOD

2.3.1 *Hot Spot Type A and B*

High stress singularities may appear along for a geometry with sharp weld corners, such as the simplified weld end of a cover plate(figure 2.1).

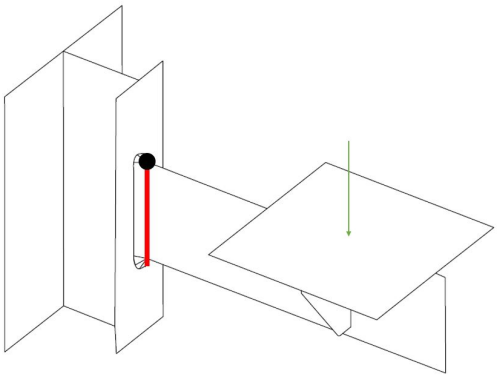

Figure 2.1: Typical hot spot type B

As shown in figure 2.1, the crack is expected to initiate from the tip of the weld(at the black dot) and propagate along the red path. If only eq. 2.27 and eq. 2.28 are applied to determine the structural stress, the peak value at the exact crack location(weld tip) will perform numerical instability(figure 2.2).

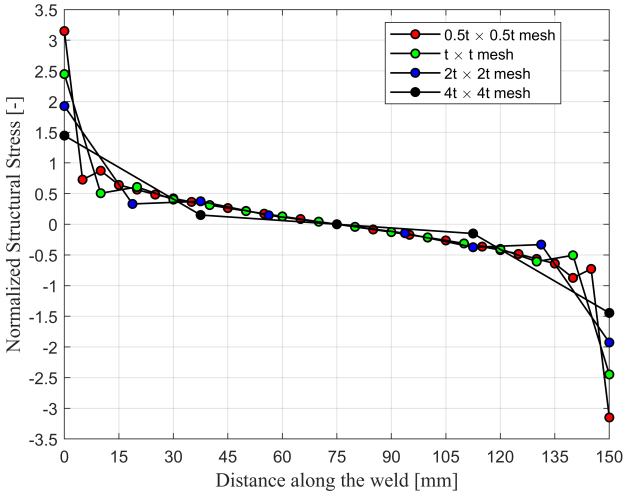

Figure 2.2: Numerical instability at the weld tip

A technique known as the GVNM has been proposed to compensate the stress singularity and smooth out the along-weld structural stress. It is essential for symmetric weld ends, that is load carrying side, and for screening using stress evaluation lines cutting across a weld end.

For hot spot type B, the stress calculated at the weld line's tip is only relevant to weld initiation, and the average stress distribution across the anticipated crack depth(l_1) is more appropriate to represent structural stress level.

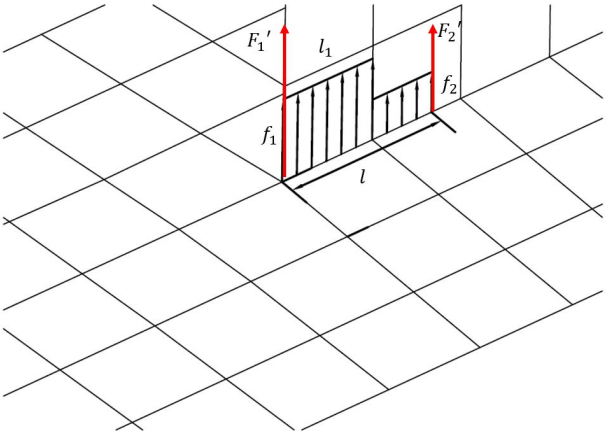

Figure 2.3: Hot spot type B virtual node

For hot spot type A, the crack will happen at the weld end perpendicular to the weld seam, meaning in practice only weld toe notches are involved. The mesh is usually coarse in that region and the high stress gradients around the weld tip location are not effectively captured along the stress evaluation line. The GVNM provides a globally accurate representation of average stresses at the crack region and outside of it.

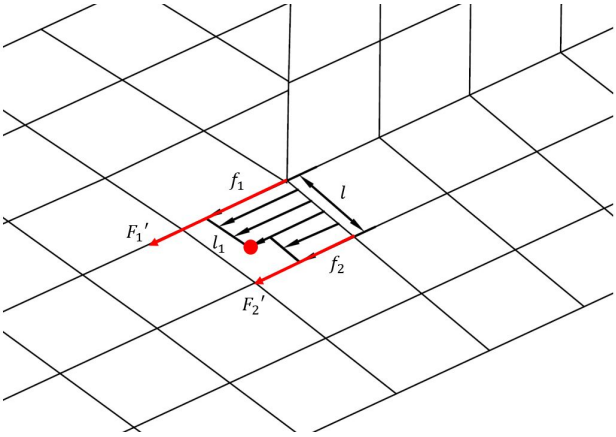

Figure 2.4: Hot spot type A virtual node

With the virtual node approach, the work equilibrium system and conservation is solved first in the same way for all nodal values of the line forces(eq. 2.28). Along a potential crack path, assumed crack length l_1 and reference length l are defined. For all types of hot spot, the structure fails when the length of the fracture reaches the plate's thickness. Therefore, it is determined that the assumed crack length is equal to the plate thickness. Reference length l defines the influence region of the hot spot. For the case of virtual node at hot spot type B, the situation is depicted as figure 2.5.

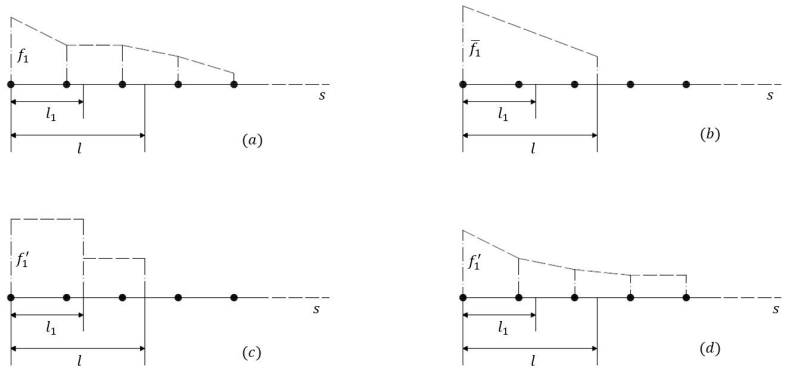

Figure 2.5: virtual node effect on assumed line force distribution, (a) original, (b) linearized, (c) enforced, (d) final distribution

The initial line force distribution is shown in figure 2.5(a) and an equivalent assumed linear line force distribution is assumed in figure 2.5(b). This is further converted to the equivalent assumed distribution in figure 2.5(c) and then reconstructed as presented in figure 2.5(d). At last the effective line force at crack initiation point is taken as f_1' instead of f_1 based on eq. 2.28, and that line forces are redistributed to preserve global virtual work equilibrium on the nodes outside of the crack region l_1.

From figure 2.5(a) to (b), the virtual displacements compatible with the linear distribution are:

$$\delta\bar{u} = (1-\eta)\delta\bar{U}_1 + \eta\delta\bar{U}_2 \text{ for } \eta \in [0,1] \tag{2.29}$$

corresponding to the curvilinear abscissa $s = \eta l$, and the equivalence of figure 2.5(a) and (b) is:

$$\int_0^l \delta\bar{u} f(s) ds = \int_0^l \delta\bar{u} \bar{f}(s) \mathrm{d}s \tag{2.30}$$

Where $f(s)$ is the line force distribution as in figure 2.5(a) obtained by eq. 2.27. From the virtual work principle, this should be true for all compatible virtual displacements in eq. 2.29. By substituting equation eq. 2.29 into eq. 2.30 and expressing the identities for all possible end displacements $\delta\bar{U}_i$, two equations can be obtained to define the representation $\bar{f}(s) = (1-\eta)\bar{f}_1 + \eta\bar{f}_2$ from figure 2.5(b) :

$$\begin{aligned} &\begin{bmatrix} l\int_0^1 (1-\eta)^2 d\eta & l\int_0^1 \eta(1-\eta) d\eta \\ l\int_0^1 \eta(1-\eta) d\eta & l\int_0^1 \eta^2 d\eta \end{bmatrix} \begin{bmatrix} \bar{f}_1 \\ \bar{f}_2 \end{bmatrix} \\ &= \begin{bmatrix} \int_0^l (1-s/l) f(s) ds \\ \int_0^l (s/l) f(s) ds \end{bmatrix} \end{aligned} \tag{2.31}$$

The average line force of kth segment f_{avk} is calculated by the local abscissa along the curve with origin at node 1:

$$f_{avk} = \frac{f(x_{k+1}) + f(x_k)}{2} \tag{2.32}$$

Based on trapz relation, the membrane component of the line force over l is expressed as:

$$f_{ml} = \sum_{k=1}^{N} \frac{(x_{k+1} - x_k) \cdot f_{avk}}{L} \tag{2.33}$$

The line force/moment indicator $f(s)$ is linearly distributed over each segment along the stress evaluation line. Hence, $f(s)$ is assumed to be:

$$f(s) = a_k s + b_k \tag{2.34}$$

where a_k and b_k are the slope and intercept of the line force/moment distribution of the kth segment. s is the local coordinates within kth segment.

$$a_k = \frac{f(x_{k+1}) - f(x_k)}{x_{k+1} - x_k} \tag{2.35}$$

$$b_k = f(x_k) - \frac{f(x_{k+1}) - f(x_k)}{x_{k+1} - x_k} \cdot x_k \tag{2.36}$$

The bending component of the linearized line force over l_1 is:

$$f_{bl} = \sum_{k=1}^{N} (a_k/3 \cdot s^3 + b_k/2 \cdot s^2)|_{x_k}^{x_{k+1}} \tag{2.37}$$

$\bar{f}_1$ and $\bar{f}_2$ are calculated by:

$$\begin{bmatrix} \bar{f}_1 \\ \bar{f}_2 \end{bmatrix} = \begin{bmatrix} f_{ml} + f_{bl} \\ f_{ml} - f_{bl} \end{bmatrix} \tag{2.38}$$

With this line force distribution we may calculate the equivalent nodal forces at each end of the reference length l using the equivalence:

$$\begin{bmatrix} F_1' \\ F_2' \end{bmatrix} = \frac{l}{6} \begin{bmatrix} 2 & 1 \\ 1 & 2 \end{bmatrix} \begin{bmatrix} \bar{f}_1 \\ \bar{f}_2 \end{bmatrix} \tag{2.39}$$

It can be noticed that the right hand side of eq. 2.29 is identical to the left of eq. 2.39, which indicates that the equivalent nodal forces F_1' and F_2' can just be calculated implicitly by the right of eq. 2.29. The reformed equation becomes:

$$\begin{bmatrix} F_1' \\ F_2' \end{bmatrix} = \begin{bmatrix} \int_0^l (1 - s/l) f(s) ds \\ \int_0^l (s/l) f(s) ds \end{bmatrix} \tag{2.40}$$

Therefore, eq.2.40 becomes:

$$\begin{aligned} \begin{bmatrix} F_1' \\ F_2' \end{bmatrix} &= \begin{bmatrix} \int_0^l (1 - s/l) \cdot (a_k s + b_k)\, \mathrm{d}s \\ \int_0^l (s/l) \cdot (a_k s + b_k)\, \mathrm{d}s \end{bmatrix} \\ &= \begin{bmatrix} \sum_{k=1}^{N} \left[a_k/2 \cdot s^2 + b_k \cdot s - \right. \\ \left(a_k/3 \cdot s^3 + b_k/2 \cdot s^2 \right) / \, l |_{x_k}^{x_{k+1}} \\ \sum_{k=1}^{N} \left(a_k/3 \cdot s^3 + b_k/2 \cdot s^2 \right) / \, l |_{x_k}^{x_{k+1}} \end{bmatrix} \end{aligned} \tag{2.41}$$

The line force representation in figure 2.5(c) can then be solved for by building static equilibrium at both ends of the segment:

$$f_1' = \frac{F_1'(l_1 + l) + F_2'(l_1 - l)}{l_1 l} \tag{2.42}$$

$$f_2' = \frac{F_2'(2l - l_1) - F_1' l_1}{(l - l_1) l} \tag{2.43}$$

Yielding the system of equations:

$$\frac{1}{2l}\begin{bmatrix} l_1(2l - l_1) & (l - l_1)^2 \\ l_1^2 & l^2 - l_1^2 \end{bmatrix}\begin{bmatrix} f_1' \\ f_2' \end{bmatrix} = \begin{bmatrix} F_1' \\ F_2' \end{bmatrix} \tag{2.44}$$

The above system is not symmetrical since the virtual displacements and the assumed line forces are not in duality. However, the virtual work equilibrium is preserved for the assumed virtual displacements when changing from the scheme in figure 2.5(a) to the discontinuous representation figure 2.5(c). The corresponding line moment redistribution at the same location can be calculated based on the same method. The new line force and moment along the weld considering the weld end effect can be obtained by resolving eq. 2.27, with the line forces and moment at the weld tip as constraints. The Python command "*lsq_linear*" with "*bvls*" method is used to optimize the stress distribution.

To examine the mesh sensitivity, six drastically different mesh sizes from $0.125t \times 0.125t$ to $4t \times 4t$ are used in the mesh designs. The distance l_1 is set equal to the plate thickness $10mm$, which is the same as Dong (2005). The reference length has a requirement of $l \geq 2l_1$:

$$l_1 = \begin{cases} l_e & l_e \geq l_1 \\ t_p & l_e \leq l_1 \end{cases} \tag{2.45}$$

The normalized structural stress distribution along the weld is plotted in figure 2.6. The peak value at the crack location converged for

different mesh sizes, varying from 1.58 to 1.62. However, If there are multiple nodes located within the reference length l_1($0.125t \times 0.125t$ to $0.5t \times 0.5t$), non-monotonic behavior still appears within the l_1 distance. Therefore, simply limiting the weld tip nodal results is insufficient to help fine mesh results converge.

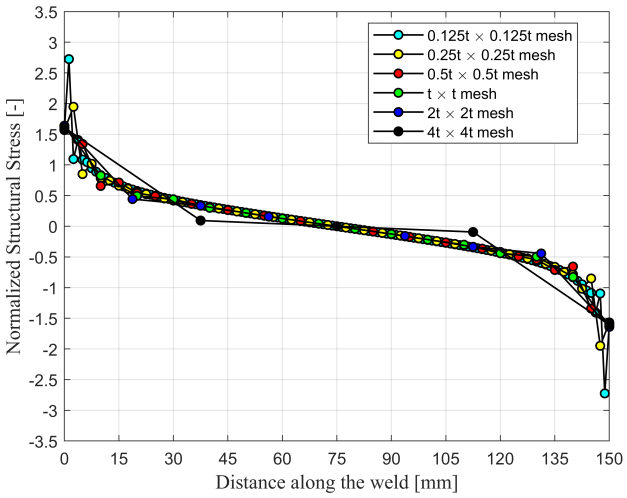

Figure 2.6: Comparison of structural stress distribution along weld toe on the attachment plate

2.3.2 l_1 *Linearization*

In order to further smooth the stress distribution with multiple elements located within l_1, there is a case globally re-equilibrating the virtual work equilibrium for the complete set of virtual displacements constrained by the stress distribution along the assumed crack length l_1.

A monotonic linear line force distribution can be applied to generate the equivalent line forces at nodes within the interval defined

by l_1. The gradient of equivalent line force over l_1 is the same to the gradient of figure 2.5(b) over l. The slope $\bar{m}$ can be written as:

$$\bar{m} = \frac{\bar{f}_1 - \bar{f}_2}{x_l - x_0} \tag{2.46}$$

where $\bar{f}_1$ and $\bar{f}_2$ are the linearized line forces at the weld tip and reference length l location. Hence, the line forces over l_1 distribution can be determined by f_1' and slope $\bar{m}$, except that line forces at the nodes past the distance l_1 also depend on the unknown solution beyond. This will be taken care of naturally by the remainder of the equations in the system eq. 2.28. More precisely, partitioning the equilibrium eq. 2.28in the form:

$$\begin{bmatrix} \mathbf{F}_c \\ \mathbf{F}_a \end{bmatrix} = \begin{bmatrix} Q_{cc} & Q_{ca} \\ Q_{ac} & Q_{aa} \end{bmatrix} \begin{bmatrix} \mathbf{f}_c' \\ \mathbf{f}_a' \end{bmatrix} \tag{2.47}$$

Where index c refers to the set of nodes 1 to $n-1$ within the crack length l_1, and the transformation matrix Q is the same as eq. 2.28. The k^{th} node is excluded from index c when it is just at the l_1 location. The line force $\mathbf{f}_c'$ is the linearized results over l_1 and $\mathbf{f}_a'$ is the optimized results with index c constrained. $\mathbf{F}_c$ and $\mathbf{F}_a$ are the nodal forces along the weld corresponding to nodes in index c and a. Finally, when conditions such as virtual node are specified at both ends of the stress evaluation line, it is an easy matter to adapt the above procedures by appropriate partitioning and reordering of the equilibrium equations.The stress distribution will then look as shown in figure 2.7.

It can be noted that the peak stress shows at the end of the weld converged from 0.125t to 4t mesh sizes, with all results below 2.5% deviation. The stress distribution illustrated a monotonic behavior with linearized stress results within l_1 distance from $0.125t \times 0.125t$ to $t \times t$ model. For 4t mesh size, the stress distribution line is no more falling on the data clouds, because there are only 4 elements along the weld. However, the peak stress is still converging at the same results.

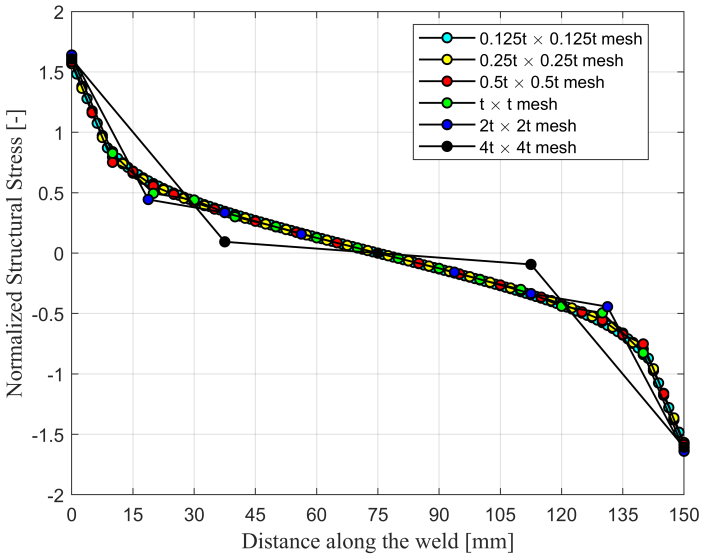

Figure 2.7: Comparison of structural stress distribution along weld toe on the attachment plate with constraints within l_1 using linearization over l_1

2.3.3 *Savitzky–Golay Filter*

As illustrated in figure 2.2 and 2.6, it can be highlighted that only the first three nodes indicate the most non-monotonic behavior. Therefore, a Savitzky-Golay Filter can be used to re-establish the virtual work equilibrium for the entire collection of virtual displacements confined by the assumed linear stress distribution for the first three nodes at the weld end. In this case, only at maximum of three nodes would be constrained.

The stress results of the first three nodes can be solved by a linear distribution mentioned in 2.3.2. Then the line force along the weld is re-equilibrated by eq.2.47. In this stage, the numerical instability is stablized into a lower level to avoid over-filtering of Savitzky–Golay filter. Finally, the Savitzky–Golay filter is applied over the whole

weld. A polynomial order of 3 is applied and the frame length is determined to be 7. The stress distribution along weld with different mesh size is shown below:

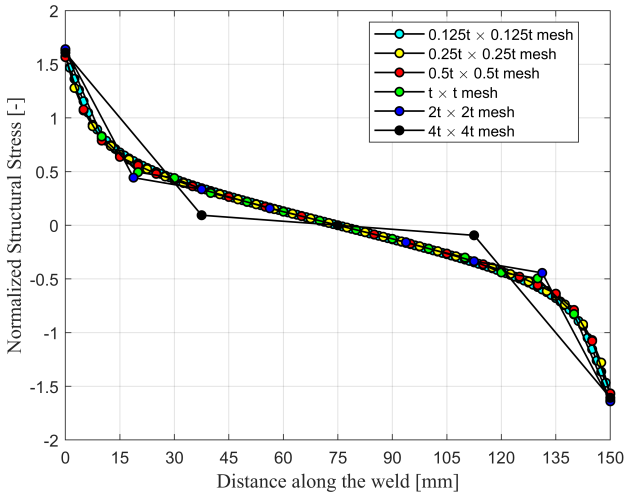

Figure 2.8: Comparison of structural stress distribution along weld toe on the attachment plate with constraints within l_1 with Savitzky–Golay filter

It can be noticed that Savitzky–Golay filter gives a more smooth transition at l_1 location than the linearization over l_1 approach. However, Savitzky–Golay filter results are sensitive to pre-determined frame length. If frame length is too small, the line force results can be easily over filtered, which may influence the weld tip results. If the frame length is too large, the numerical instability will not be fully smoothed.

2.3.4 *Peak Stress At The Other Side of The Bracket End*

For the model shown in figure 2.1, there will be a sharp increase of stress results at the other side of the bracket end.

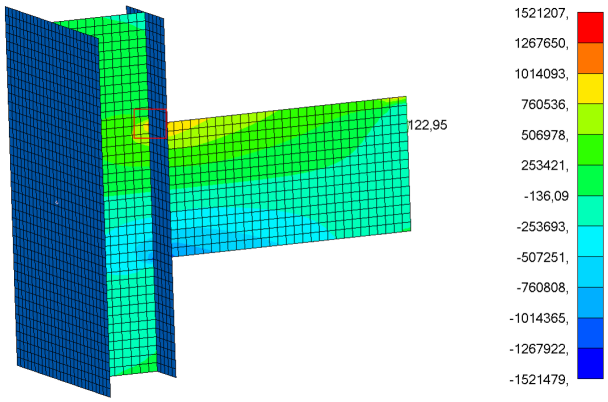

Figure 2.9: The other side of the bracket end

Based on eq. 2.28, the Battelle structural stress for models with different mesh sizes are plotted in the figure below:

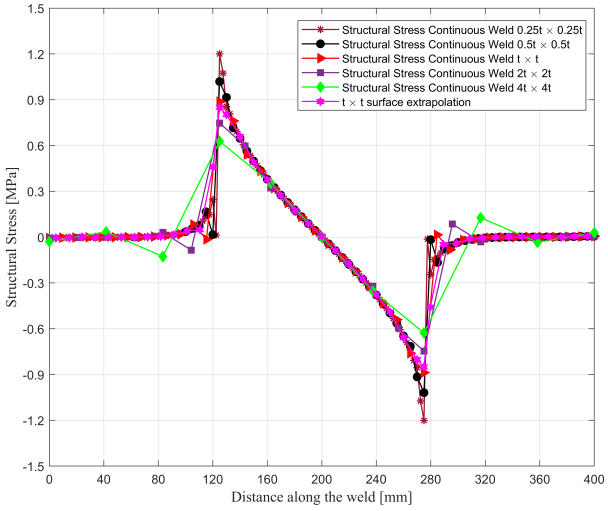

Figure 2.10: The other side of the bracket end Battelle structural stress with different mesh sizes

A similar non-convergent phenomenon appears at the peak stress location. Therefore, the virtual node method could also be applied

to redistribute the stress distribution around the other side of the bracket end. The 3-point generalized virtual node method for this specific example is calculated as depicted in figure 2.11.

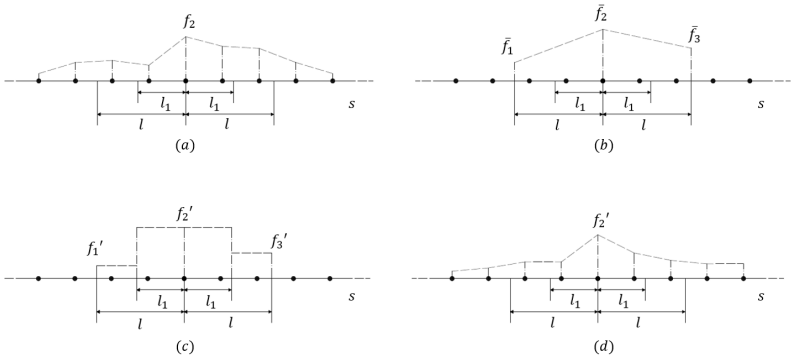

Figure 2.11: 3 point generalized virtual node method

l and l_1 follow the relation in eq. 2.45. Figure 2.13(a) is the initial line force results calculated by eq. 2.28. Figure 2.13(b) shows the equivalent linearized line force over l. The right hand side linearized line force $\bar{f}_2^R$ and left hand side linearized line force $\bar{f}_2^L$(figure 2.12) are both calculated by eq. 2.32 to eq. 2.38. f_2 used for linearization on both sides is the results calculated by eq. 2.28.

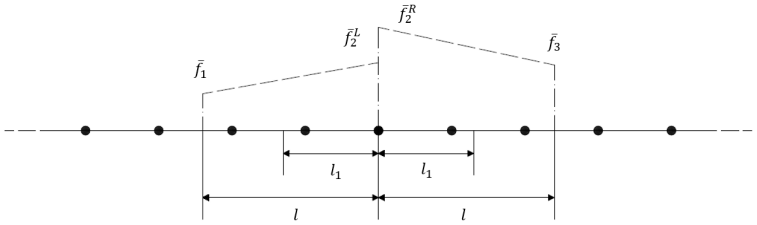

Figure 2.12: GVNM left hand side and right hand side $\bar{f}_2$

$\bar{f}_2$ is the linear superposition of $\bar{f}_2^R$ and $\bar{f}_2^L$.

$$\bar{f}_2 = \bar{f}_2^R + \bar{f}_2^L \tag{2.48}$$

$\bar{f}_1$, $\bar{f}_2$ and $\bar{f}_3$ are further converted to figure 2.11(c) by static equilibrium:

$$F_1' + F_2' + F_3' = f_1' \cdot (l - l_1) + f_2' \cdot (2 \cdot l) + f_3' \cdot (l - l_1) \tag{2.49}$$

$$F_1' \cdot l - F_3' \cdot l = \frac{f_1' \cdot (l - l_1) \cdot (l + l_1)}{2} - \frac{f_3' \cdot (l - l_1) \cdot (l + l_1)}{2} \tag{2.50}$$

$$F_2' \cdot l + F_3' \cdot 2 \cdot l = f_2' \cdot 2 \cdot l^2 + f_3' \cdot (l - l_1) \cdot \left(l + \frac{(l - l_1)}{2} \right) \tag{2.51}$$

Therefore, the effective line force f_2' is solved as:

$$\begin{aligned} f_2' = & \frac{3F_1'l^2 - 4F_1'll_1 + F_1'l_1^2 + F_2'l^2 + 2F_2'l_1}{2l\left(l^2 + 2ll_1 + l_1^2\right)} + \\ & \frac{F_2'l_1^2 - F_3'l^2 + 8F_3'l_1 + F_3'l_1^2}{2l\left(l^2 + 2ll_1 + l_1^2\right)} \end{aligned} \tag{2.52}$$

The Battelle structural stress distribution of element size $0.25t \times 0.25t$ to $4t \times 4t$ are all plotted in figure 2.13 to clarify their difference.

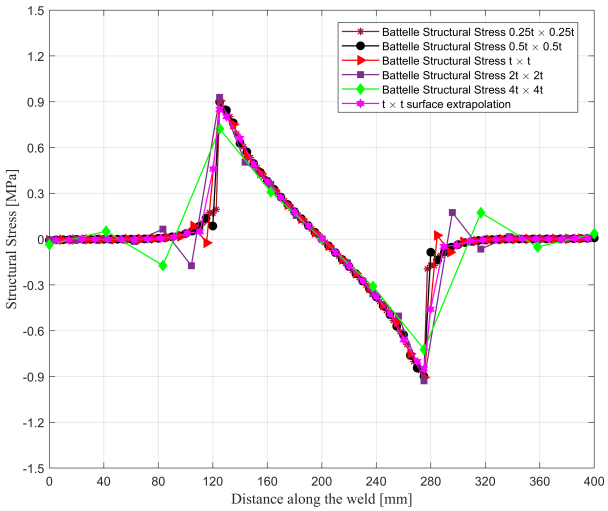

Figure 2.13: The other side of the bracket end Battelle structural stress with GVNM

The peak stress is converged for models with mesh sizes from $0.25t \times 0.25t$ to $2t \times 2t$. Compared with hot spot structural stress, the overall stress distribution is very similar. However, the peak stress of $4t \times 4t$ is lower than other models. There are only 3 elements on one side of the bracket end location (figure 2.14) and hence too coarse to accurately capture the peak values.

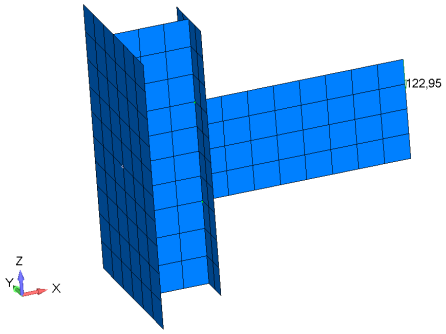

Figure 2.14: The other side of the bracket end $4t \times 4t$ element size model

It should be highlighted that the l_1 linearization should also be applied for models with mesh sizes smaller than l_1. $\bar{f}_2/2$ (instead of $\bar{f}_2$) and $\bar{f}_3$ are used to calculate the gradient of stress distribution on the right hand side of the peak stress shown in figure 2.11(b). Furthermore, l_1 linearization is only applied in the region of 125mm to 135mm and 265mm to 275mm. No additional constraint is added in 115mm to 125mm and 275mm to 285mm. Currently, there is no applicable method found for calculating the gradient of structural stress within l_1 on the side where stress increases sharply. According to figure 2.13, the spiky behavior becomes pretty obvious for mesh sizes larger than $0.5t \times 0.5t$ in the region of 125mm to 135mm and 265mm to 275mm. This is because the mesh is insufficiently fine to capture the gradient of the abrupt stress increase over a very short distance.

2.4 VERIFICATION

2.4.1 *Hot Spot Type B*

To verify the structural stress results along the weld, the DNV-GL hot spot type B verification model was established and compared. The geometry dimensions are shown in the figure 2.15:

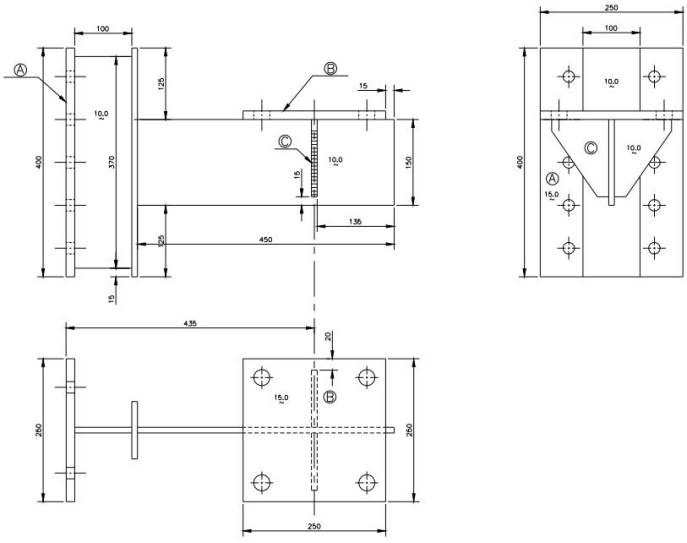

Figure 2.15: Geometries of DNV-GL hot spot type B verification model

The model was set up to produce a 1MPa nominal stress at the hot spot location when 123N force was applied on the top square plate with 250mm width. The extra stiffened panels will not affect the FEM results. Hence, the FEM model was simplified into the model shown in figure below:

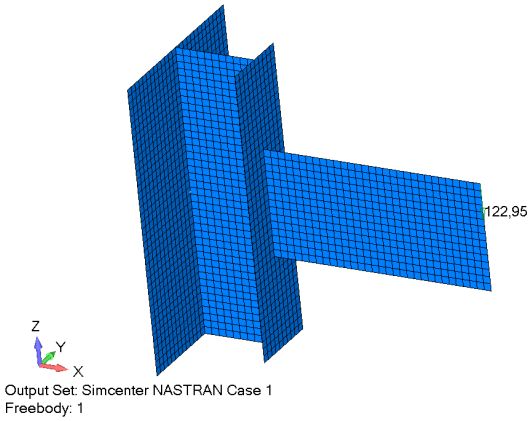

Figure 2.16: FEM DNV-GL hot spot type B verification model

The results of Battelle structural stress and hot spot structural stress are shown in one plot as comparisons.

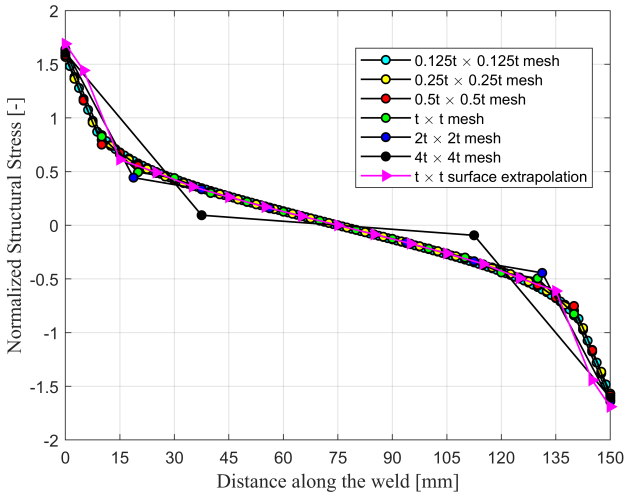

Figure 2.17: Battelle structural stress and hot spot structural stress results comparisons

The hot spot structural stress is captured with a $t \times t$ mesh model through surface extrapolation. The mesh is all made up of 4-node quad elements. Linear surface extrapolation method was based on principal stresses from two nodes on the surface at 0.5t and 1.5t from the weld toe. For the $t \times t$ mesh model, the elemental stress is the stress value at the center of the element, which is an average value of stresses at the four corners. Hence, the stress value that 0.5t and 1.5t away from the notch is taken at the center of the first and second layer of elements near the weld.

It can be seen that the Battelle structural stress and the hot spot structural stress along the weld coincide extremely well. However, the peak value of the hot spot structural stress is slightly higher at the hot spot type B location, differing by 4% from the Battelle structural stress (1.69 for hot spot structural stress and 1.62 for Battelle structural stress).

To visualize the stress distribution along the weld, the structural stress was plotted with different mesh sizes. From figure 2.18 to figure 2.25, the contour plot of structural stress and perpendicular to the weld elemental stress are displayed. The structural stress distribution is uniform among all mesh sizes. In comparison to the elemental stress, the Battelle structural stress exhibits a fairly comparable color contour along the weld, indicating its good precision.

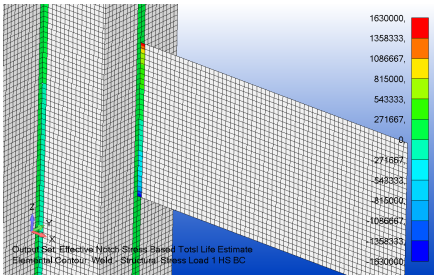

Figure 2.18: Structural stress $0.5t \times 0.5t$

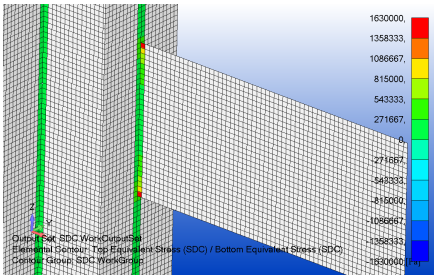

Figure 2.19: Elemental stress $0.5t \times 0.5t$

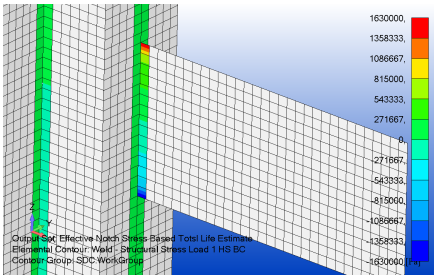

Figure 2.20: Structural stress $t \times t$

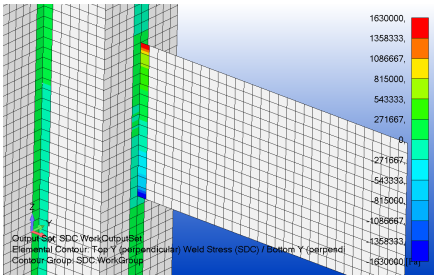

Figure 2.21: Elemental stress $t \times t$

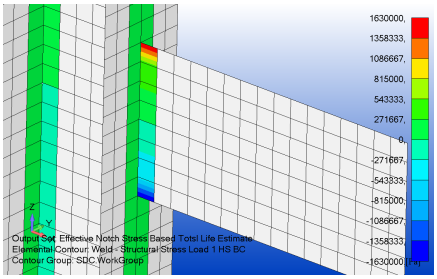

Figure 2.22: Structural stress $2t \times 2t$

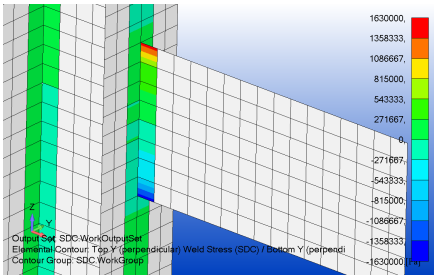

Figure 2.23: Elemental stress $2t \times 2t$

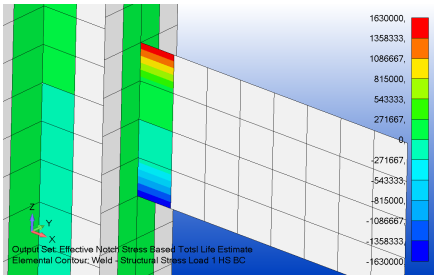

Figure 2.24: Structural stress $4t \times 4t$

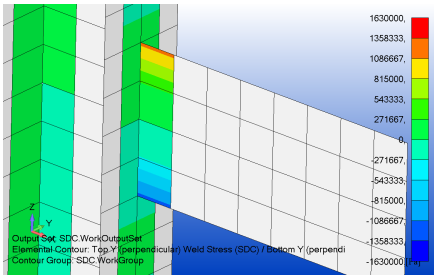

Figure 2.25: Elemental stress $4t \times 4t$

2.4.2 *Hot Spot Type C*

Regarding Lee *et al.* (2010)'s research, a separate stiffened panel model was created in order to better test the results of the hot spot

type C structural stress. The geometric details are displayed in figure 2.26

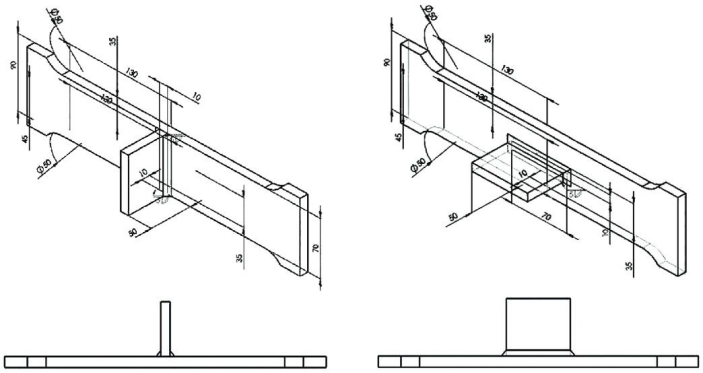

Figure 2.26: Hot spot type C and A verification model(Lee *et al.*, 2010)

The hot spot type C model is evaluated using two distinct load cases and four different mesh sizes, ranging from 0.25t to 2t. The first load case is pure tensile with a 29.4kN force applied on the specimen(figure 2.27). The second load case is 3-point bending with a 68.6kN force added at the center of the specimen(figure 2.28).

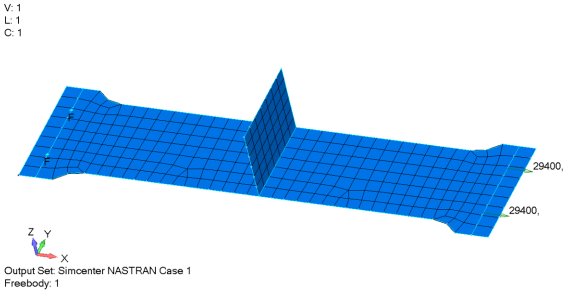

Figure 2.27: Hot spot C tensile load and constraints

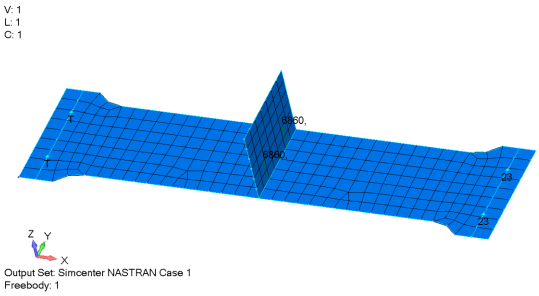

Figure 2.28: Hot spot C bending load and constraints

The Battelle structural stress was calculated by eq. 2.28 without GVNM, and hot spot structural stress comparison were obtained through linear surface extrapolation.

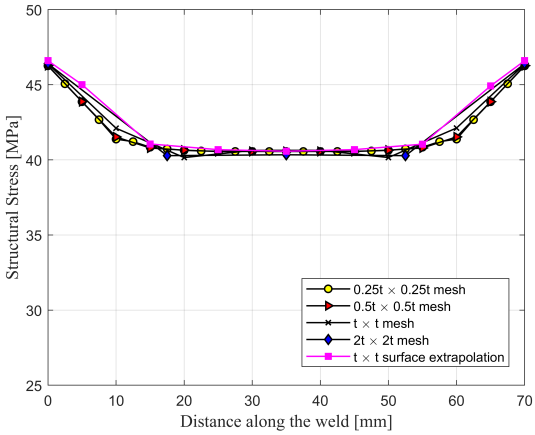

Figure 2.29: Hot spot C Battelle and hot spot structural stress comparison with tensile load

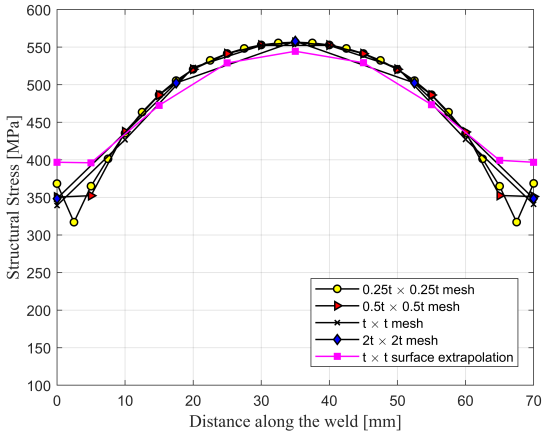

Figure 2.30: Hot spot C Battelle and hot spot structural stress comparison with bending load

According to figure 2.29, the Battelle structural stresses for all mesh sizes are extremely close to the linear surface extrapolation hot spot structural stress of mesh size $t \times t$. For the 3-point bending specimen, the results of the two models along the weld are also fairly similar(figure 2.30). Still convergent along the hot spot type C notch, the Battelle stress results are 14% less than the hot spot structural stress values.

2.4.3 *Hot Spot Type A*

Based on Dong (2005)'s finding, the Battelle structural stress of hot spot type A is supposed to be calculated by the generalized virtual node method due to the weld tip influence. Therefore, a separate stiffened panel model is needed to verify the type A hot spot results. The specimen was tested under a horizontal tensile load of 29.4kN, making the weld tip of the gusset a hot spot type A. According to chapter 2.3, eq. 2.42 is employed for the redistribution of the line force, and eq. 2.28 was used to calculate the Battelle the structural stress at the weld tip.

Based on the assumption of generalized virtual node method, the mesh size should be larger than $l_1 = 0.5t_p + l_w = 10mm$. According to the experimental detail, the average leg length of the base plate and the gusset side are 5.0 mm, respectively. Hence, the element size was determined to be 17.5mm, 26mm and 35mm in the FEM model(figure 2.31, 2.32 and 2.33):

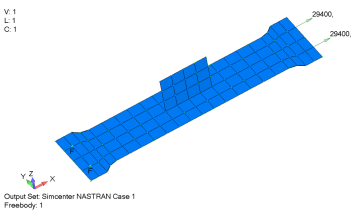

Figure 2.31: Hot spot A 17.5mm

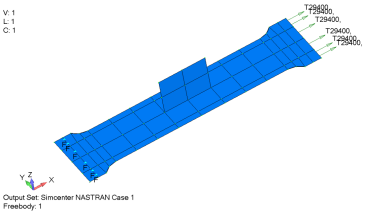

Figure 2.32: Hot spot A 26mm mesh

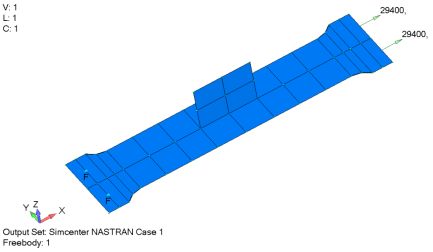

Figure 2.33: Hot spot A 35mm mesh

The Battelle structural stress and hot spot structural stress comparison is shown in table below:

Table 2.2: Hot spot A structural stress comparisons

Mesh size[mm]	Battelle[MPa]	Surface Extrapolation[MPa]
10	-	49.98
17.5	53.48	-
26	53.11	-
35	51.02	-

It is clear that the mesh sizes 17.5mm and 26mm generate fairly similar results. Nonetheless, the disparity becomes greater in the 35mm mesh model, which may be due to the definition of the reference length. The l distance is a local geometry parameter and is therefore not intended to exceed half the plate's width(figure 2.33). For the 35mm mesh model, the single element in the plate width direction cannot capture the bending component, since the nodal moments of the two nodes we employ are always exactly opposite.

2.4.4 *Weld Separation Influence*

The structural stress requires all the nodal forces and moments to form the matrix calculation in eq.2.28. However, the weld will be separated to simplify the recognition procedure. As shown in figure below, the highlighted weld were separated due to T joint/cruciform joint recognition. Therefore, it is necessary to estimate the influence caused by weld separation effect.

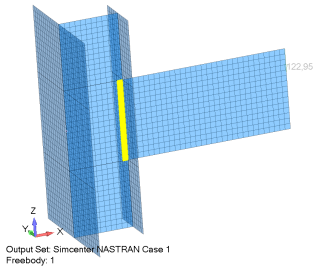

Figure 2.34: Weld center part separation

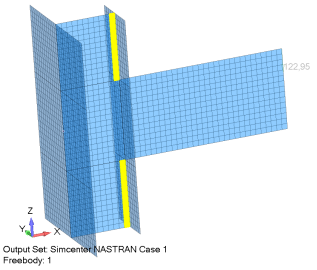

Figure 2.35: Weld side part separation

The data used to verify the results is from the $t \times t$ mesh model. The structural stress of the continuous weld was first calculated. Then the structural stress of the three separated weld part were also plotted as comparison. As shown in figure 2.36 and 2.37, the structural stress is very comparable to each other.

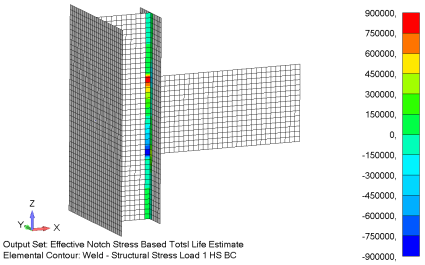

Figure 2.36: Continuous structural stress

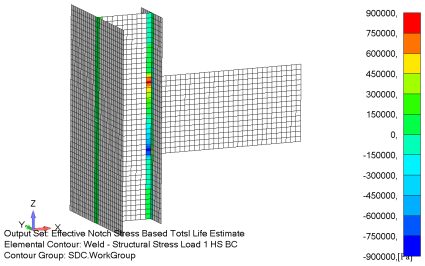

Figure 2.37: Separated structural stress

In order to clearly identify the difference between the continuous and separated calculation, the structural stress distribution of continuous weld, separated weld and hot spot structural stress is shown below:

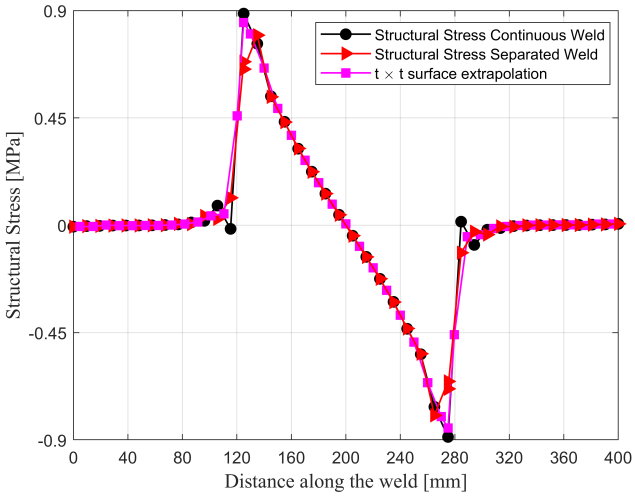

Figure 2.38: Comparisons of structural stress with continuous weld and separated weld

It can be noticed that the Battelle structural stress calculated by continuous weld is comparable to the separated counterpart along most part of the weld. However, the peak stress value along the

weld is not the same for the two approach. The continuous weld results(0.877MPa) is 7.8% higher than the separated weld structural stress results(0.796MPa). It likely results from the discrepancy in nodal forces and nodal moments. For the Battelle structural stress calculation, the nodal forces and moments are summed at node I from the adjacent weld toe components located on the positive side of the weld direction. Therefore, at the site of the hot spot, the nodal forces and moments of the continuous weld are greater than those of the separated weld, which accounted for the contribution of only one element. Due to separation, the transformation matrix for separated/continuous weld is also different, which may result in deviations. The structural stress predicted by the separated weld model is more comparable to the hot spot structural stress based on linear surface extrapolation than its continuous counterpart.

The continuous and separated weld comparison from 0.5t to 4t mesh size is plotted in one figure below:

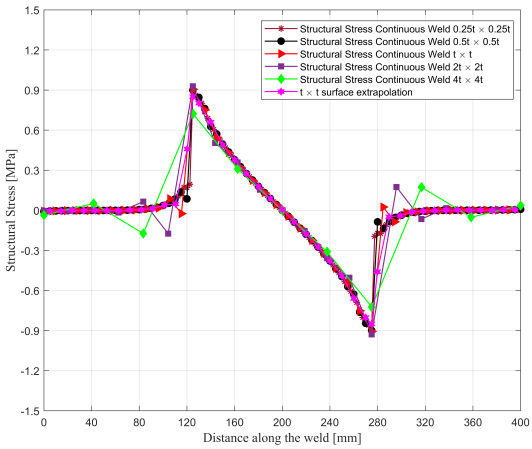

Figure 2.39: Comparisons of continuous weld Battelle structural stress with different mesh sizes

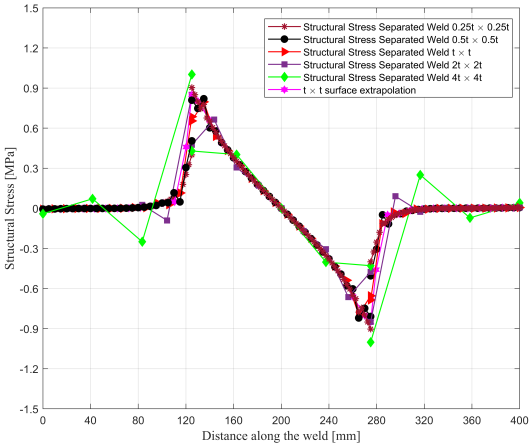

Figure 2.40: Comparisons of separated weld Battelle structural stress with different mesh sizes

Overall, the structural stress at the break point of separated weld is not converged for all mesh sizes. The difference of 0mm to 125mm weld and 125mm to 275mm weld is pretty low for $t \times t$ model and increases significantly for others. Compared with the continuous weld structural stress for $2t \times 2t$ and $4t \times 4t$, the separated results shows a even higher spikes at around 120mm and 270mm point. It might be caused by the smaller element number per weld compared with the continuous models. On the other hand, the stress results will be more stable if the element number is large enough. For smaller mesh sizes like $t \times t$ and $0.5t \times 0.5t$, the spikes are as small as the continuous counterpart.

If the average value of the structural stress at the break point is taken for 0mm to 125mm weld and 125mm to 275mm weld(figure 2.41), the results will be more converged than figure 2.40. However, the maximum stress location will shift to the nearby node for element sizes equal and smaller than $t \times t$. In conclusion, the Battelle structural stress calculated by separated weld approach is not accurate. Redistributing the nodal forces for 0mm to 125mm weld and 125mm to 275mm weld may help solve the problem. However, there is no

information regarding the redistribution of nodal force in the middle of a weld.

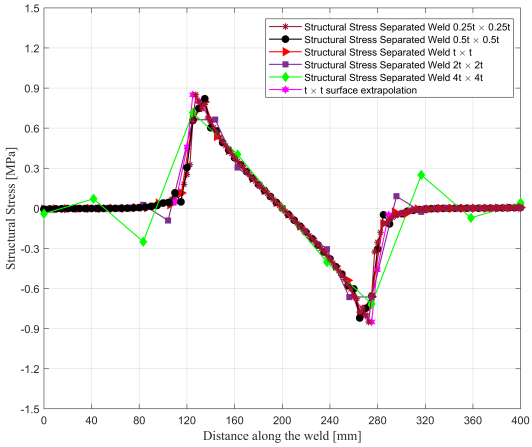

Figure 2.41: Comparisons of separated weld Battelle structural stress with different mesh sizes average on the break point

2.5 MESH QUALITY STUDY

2.5.1 *Hot Spot Type C*

The 3-point bending model and pure tensile model are first chosen to apply a mesh quality study. All the elements along the weld are randomly modified to examine the influence of ugly mesh. The average Jocobian value is 0.74 and the internal angle is 60.46.

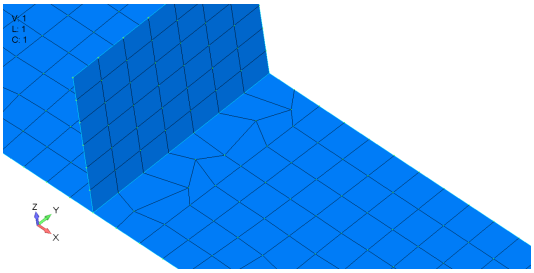

Figure 2.42: Hot spot type C mesh quality study

The comparison of $t \times t$ fine mesh and hot spot structural stress is plotted in the figure below:

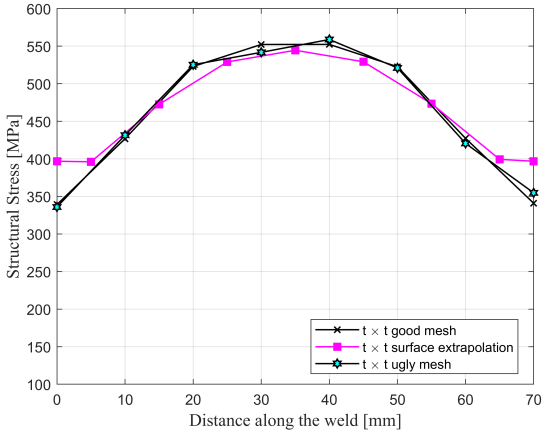

Figure 2.43: Hot spot type C mesh quality study 3-point bending

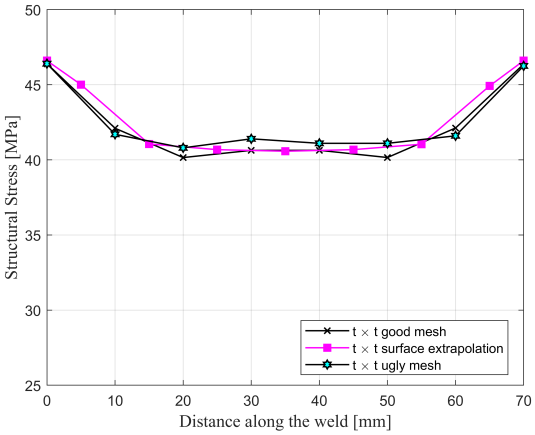

Figure 2.44: Hot spot type C mesh quality study pure tensile

It can be observed that there is hardly an influence on the Battelle structural stress. The difference between coarse mesh and fine mesh is below 1%.

2.5.2 *Hot Spot Type A*

In order to check the mesh quality influence of hot spot A generalized virtual node method, 5 different coarse mesh at hot spot A are modified(figure 2.46 to 2.50). The "top shrink" model was made to test the influence of element aspect ratio influence. "Corner 1 shrink" and "Corner 2 shrink" were reducing the element area by moving the top corner with regard to the weld tip location. The edge at the exact hot spot type A location was extended to a random location in "Corner 3 stretch" model to examine the influence of edge misalignment influence. Finally, the edge parallel to the weld seam was modified in "mesh misalign" model.

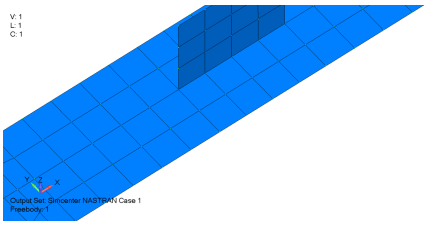

Figure 2.45: 17.5mm fine mesh

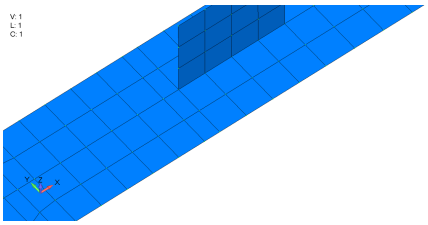

Figure 2.46: 17.5mm top shrink

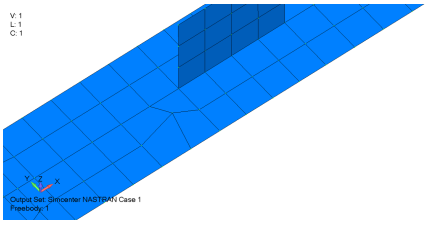

Figure 2.47: 17.5mm corner 1 shrink

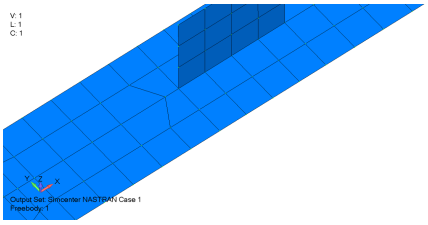

Figure 2.48: 17.5mm corner 2 shrink

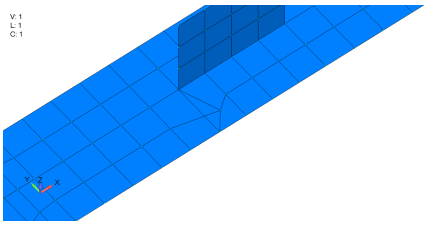

Figure 2.49: 17.5mm corner 3 stretch

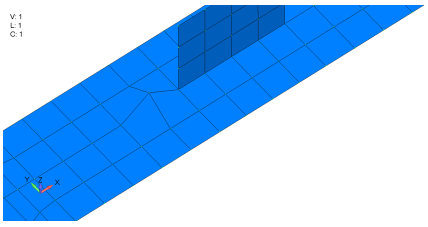

Figure 2.50: 17.5mm mesh misalign

The mesh quality of the modified elements was measured by Jocobian standard and internal angle. In the "misalign" model, the reference length l is no longer 17.5mm due to the extension of corner, and the distance between the corner and weld line $l = l_{edge} = 24.05mm$ is used instead. The results of the corresponding mesh quality are shown below:

Table 2.3: Hot spot A structural stress comparisons

	Jocobian	Internal Angles	Structural stress[MPa]
Fine mesh	0	0	53.48
Top shrink	0	0	53.23
Corner 1 shrink	0.747	61.57	59.75
Corner 2 shrink	0.54	30.665	53.2
Corner 3 Strech	0.4568	33.45	61.43
misalign	0.5102	30.2	85.1

Overall, the structural stress did not deviate much from the fine mesh results of models shown in figures 2.46 to 2.49. According to "top shrink" and "Corner 2 shrink," the along-weld modification of the top two corners parallel to the hot spot type A has no impact on structural stress. However, a random modification like figure 2.47 and 2.49 can easily cause a 10% difference. This results from the changes in nodal forces. Regarding the model shown in figure 2.47, the nodal force F_2 (which is F_2' in figure 2.4) is much smaller because of the modified corner. However, F_2 can easily be compensated by taking the average of one more element parallel to hot spot type A location(figure 2.51). The structural stress after compensation is $\sigma_s = 54.09MPa$.

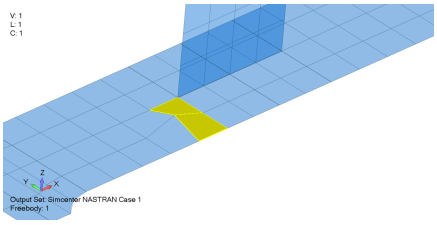

Figure 2.51: Compensation corner 1 shrink

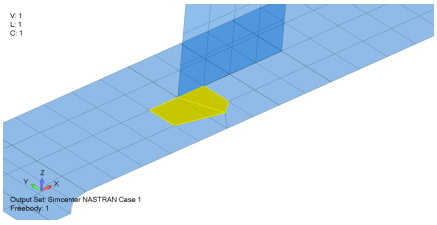

Figure 2.52: Compensation corner 3 stretch

Nodal force F_1 is much bigger in figure 2.49, which increases the Battelle structural stress in some extent. The absolute average of one

more element along the weld seam can be taken to compensate the influence, which makes the structural stress $\sigma_s = 51.8MPa$. Due to the recognition difficulty, the compensation procedures for the ugly mesh cases are not implemented in the tool.

2.6 CONCLUDING REMARKS

In this chapter, the Battelle approach to structural stress was investigated. It demonstrates great precision for various mesh sizes and mesh qualities. However, the approach does have certain restrictions. First, there is a compensation effect when there is a dramatic change in nodal forces/moments inside a very short distance. If the situation occurs in the middle of a weld, spikes will merge and the peak stress is not converged for different mesh sizes. Coarser mesh is not able to capture the gradient on the side where stress changes sharply. In addition, for hot spot type A, the ugly element with misalignment on the weld extension line causes the biggest inaccuracy. It is highly recommended to make the element edge of hot spot A be parallel to the weld extension line.

This page intentionally left blank

3

EFFECTIVE NOTCH STRESS BASED TOTAL LIFE ESTIMATE

The initial phase of crack formation makes up the the initiation fatigue lifetime of a notched structural element, followed by a period of fracture growth until eventual failure. As long as the crack growth process depends on the surface state, the first micro-crack should still be in the initiation phase. When the propagation predominantly depends on the material's resistance to crack growth, the crack growth period begins. The stress intensity factor and fracture mechanics have a larger role in the crack growth phase. However, there is a clear issue even though the transition between the two periods seems to be physically sound. How to identify the point at which the crack initiation period changes into the growth period remains mystery. The transformation would occur gradually rather than abruptly. In this case, the one-parameter effective notch stress based total life estimate is able to provide a smooth transition from crack initiation to growth(H. den Besten, 2018).

Outline The structural stress discussed in Chapter 2 is the linear stress distribution along the plate thickness direction. The notch stress is the non-linear distribution along the same direction due to the geometry changes at the surface notch, which is made up of a far-field component and a non-linear self-equilibrating part. However, a linear stress analysis of a sharp corner implies a singularity with an infinite stress concentration, which is meaningless.

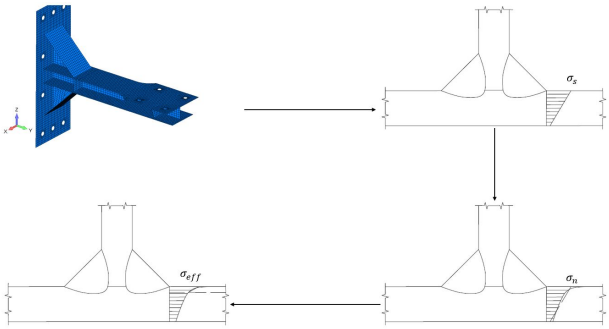

Figure 3.1: Fatigue structural stress and notch stress

The effective notch stress is based on the averaged notch stress value within ρ^*. It is representative enough for the stress level in which most of the life time is consumed. In this Chapter, the approach towards effective notch stress and total life estimate will be introduced.

3.1 WELD NOTCH STRESS DISTRIBUTION

In order to calculate the effective notch stress, a non-linear notch stress distribution is necessary to specify. The analytical notch stress distribution through the plate thickness σ_n for symmetry and non-symmetry with regard to half of the base plate thickness for both weld toe and weld root failure has already been available in J. H. den Besten (2015). The distribution will change with regard to the local geometry of the notch. The weld height h_w and weld leg length l_w are necessary to obtain an accurate notch stress through the plate thickness. Based on the geometry relation, the weld notch angle and stress angle can be expressed as:

$$\alpha = \frac{1}{2}\left\{\pi + \arctan\left(\frac{h_w}{l_w}\right)\right\} \tag{3.1}$$

$$\beta = \alpha - \frac{\pi}{2} \tag{3.2}$$

Usually in the early design stage, the dimensions of the weld are not given. It requires some engineering judgement to make some reasonable assumptions, such as $l_w = t_b$ and $h_w = t_b$.

For a weld toe notch of a T joint, the notch stress distribution can be written as:

$$\begin{aligned}\sigma_n\Big(\frac{r}{t_p}\Big) =& \sigma_s\Big\{\Big(\frac{r}{t_p}\Big)^{\lambda_s-1}\mu_s\lambda_s(\lambda_s+1)[\cos\{(\lambda_s+1)\beta\}- \\ & \chi_s\cos(\lambda_s-1)]+ \\ & \Big(\frac{r}{t_p}\Big)^{\lambda_a-1}\mu_a\lambda_a(\lambda_a+1)[\sin\{(\lambda_a+1)\beta\}- \\ & \chi_a\sin(\lambda_a-1)] + C_{bw}\cdot\Big\{2\Big(\frac{r}{t_p}\Big)-1\Big\}- \\ & 2\cdot r_s\cdot\Big(\frac{r}{t_p}\Big)\Big\}\end{aligned} \tag{3.3}$$

Coefficients μ_s and μ_a are obtained using force and moment equilibrium:

$$\mu_s = \frac{C_{bw}(\lambda_a+1)+3(\lambda_a-1)}{+(\lambda_a-\lambda_s)[\cos\{(\lambda_s+1)\beta\}-\chi_s\cos\{(\lambda_s-1)\beta\}]} \tag{3.4}$$

$$\mu_s = \frac{C_{bw}(\lambda_s+1)+3(\lambda_s-1)}{+(\lambda_a-\lambda_s)[\cos\{(\lambda_a+1)\beta\}-\chi_a\cos\{(\lambda_a-1)\beta\}]} \tag{3.5}$$

and

$$\chi_s = \frac{\cos\{(\lambda_s+1)\alpha\}}{\cos\{(\lambda_s-1)\alpha\}} \tag{3.6}$$

$$\chi_a = \frac{\sin\{(\lambda_a+1)\alpha\}}{\sin\{(\lambda_a-1)\alpha\}} \tag{3.7}$$

The eigen value λ_a and λ_s are the non-trivial system solutions, which can be found solving notch angle dependent equations respectively:

$$\left.\begin{aligned}\lambda\sin(2\alpha)+\sin(\lambda 2\alpha)=0 \\ \lambda\sin(2\alpha)-\sin(\lambda 2\alpha)=0\end{aligned}\right\}\forall(\lambda>0,\lambda\neq 1) \tag{3.8}$$

In case of symmetry(J. H. den Besten, 2015)

$$\begin{aligned}\sigma_n\left(\frac{r}{t_p}\right) =& \sigma_s\left(\left[1-2r_s\left\{1-f\left(\frac{r}{t_p}=\frac{1}{2}\right)\right\}\right] f\left(\frac{r}{t_p}\right)+\right.\\ & r_s\left\{2f\left(\frac{r}{t_p}=\frac{1}{2}\right)-1\right\}\\ & \left.\left[\left\{1-f\left(\frac{r}{t_p}=\frac{1}{2}\right)\right\}-2\left(\frac{r}{t_p}\right)\right]\right)\end{aligned} \tag{3.9}$$

with

$$\begin{aligned}f\left(\tfrac{r}{t_p}\right) = \sigma_s\Big\{&(\tfrac{r}{t_p})^{\lambda_s-1}\mu_s\lambda_s(\lambda_s+1)\left[\cos\left\{(\lambda_s+1)\,\beta\right\}-\right.\\ &\left.\chi_s\cos\left\{(\lambda_s-1)\,\beta\right\}\right]+\\ &\left(\tfrac{r}{t_p}\right)^{\lambda_a-1}\mu_a\lambda_a\left(\lambda_a+1\right)\left[\sin\left\{(\lambda_a+1)\,\beta\right\}-\right.\\ &\left.\chi_a\sin\left\{(\lambda_a-1)\,\beta\right\}\right]+\\ &C_{bw}\left\{4\left(\tfrac{r}{t_p}\right)-1\right\}-2\cdot r_s\cdot\left(\tfrac{r}{t_p}\right)\Big\}\end{aligned} \tag{3.10}$$

and

$$f\left(\frac{r}{t_p}=\frac{1}{2}\right)=\frac{\left(\lambda_a-\lambda_s\right)\left(\lambda_a\lambda_s-2C_{bw}\right)}{\lambda_a\left(\lambda_a-1\right)-\lambda_s\left(\lambda_s-1\right)}+C_{bw} \tag{3.11}$$

Plane strain conditions have been assumed, meaning 3D effects can be neglected. For HS's type C and A at the base plate $t_p = t_b$ and at the cover plate $t_p = t_c$. An artificial plate thickness $t_p = t_p{}'$ is introduced for HS's type B, which is assumed to be 20mm for all cases. r_s is the structural bending stress ratio $r_s = (\sigma_b/\sigma_s)$ based on structural stress results.

The weld geometry causes a local change in stiffness; a shift in neutral axis, meaning the weld becomes load carrying up to some extent. Considering a weld toe notch as typically encountered in a welded joint without symmetry with respect to $(t_p/2)$, a counter-clockwise bending moment is introduced for a normal line force f_n pointing to the right and a clockwise bending line moment m_b. The corresponding weld load carrying (bending) stress distribution particularly affects the zone 2 stress gradient (Eq. 18). For a weld toe

notch of a welded joint showing symmetry with respect to $(t_p/2)$ the same principle applies to the related half plate thickness.

The weld load carrying stress component is geometry $(t_b, t_c, l_w, h_w, a_n)$ and loading (f_n, m_b) dependent, meaning coefficient C_{bw} contains the notch stress distribution specific information. With respect to loading, $\sigma_s C_{bw}$ is assumed to be linear superposition of a normal force and bending moment induced structural field membrane stress and bending stress component:

$$\sigma_s C_{bw} = \sigma_m C_{bm} + \sigma_b C_{bb} \tag{3.12}$$

with

$$C_{bm} = \frac{m_{bm}}{\sigma_s (1 - r_s)} \cdot \left(\frac{6}{t_p^2} \right) \tag{3.13}$$

and

$$C_{bb} = \frac{m_{bb}}{\sigma_s r_s} \cdot \left(\frac{6}{t_p^2} \right) \tag{3.14}$$

Bending moments m_{bm} and m_{bb} are estimated using a FE beam model in order to obtain weld load carrying stress information. However, building a beam model will increase the workload in some extent in the early design stage. Alternative to a beam model-based weld load carrying stress estimate involving a physical and fitting part, a parametric fitting function has been obtained as well. For the double sided T joint:

$$\begin{aligned} C_{bm} &= 0.117 - 0.192 \cdot e^{-0.494 \cdot W} \\ &\quad + \frac{0.793 \cdot P^3 + 1.113 \cdot P^2 + 0.957 \cdot P + 0.9}{P^4 + 4.721 \cdot P^3 + 13 \cdot P^2 + 9.669 \cdot P + 9.079} \end{aligned} \tag{3.15}$$

$$\begin{aligned} C_{bb} &= 0.123 - 0.261 \cdot e^{-0.712 \cdot W} \\ &\quad + \frac{0.143 \cdot P^4 + 1.007 \cdot P^3 + 1.438 \cdot P^2 + 1.674 \cdot P + 1.578}{P^4 + 3.892 \cdot P^3 + 9.41 \cdot P^2 + 7.57 \cdot P + 8.118} \end{aligned} \tag{3.16}$$

and for the double sided cruciform joint:

$$C_{bm} = 0.015 - 0.026 \cdot e^{-0.588 \cdot W} + \frac{0.297 \cdot P + 0.22}{P^2 + 3.144 \cdot P + 4.478} \tag{3.17}$$

$$C_{bb} = 0.028 - 0.039 \cdot e^{-0.340 \cdot W} + \frac{0.044 \cdot P^2 + 0.141 \cdot P + 0.116}{P^2 + 2.881 \cdot P + 2.505} \tag{3.18}$$

with

$$W = \left(\frac{h_w}{l_w} \right) \tag{3.19}$$

$$P = \log \left(\frac{t_c/2 + l_w}{t_b} \right) \tag{3.20}$$

3.2 EFFECTIVE NOTCH STRESS

Based on the notch stress distribution along the crack path, the effective notch stress can easily obtained by integrating over the material characteristic length. By assuming a v-shaped notch at the weld location, the effective notch stress analytical solution can be calculated as:

$$\begin{aligned} \sigma_e =& \frac{1}{\rho^*} \int_0^{\rho^*} \sigma_n(r) \mathrm{d}r \\ =& \sigma_s \cdot \left(\frac{t_p}{\rho^*} \right) \cdot \left\{ \left(\frac{p^*}{t_p} \right)^{\lambda_s} \mu_s (\lambda_s + 1) \left[\cos\left\{ (\lambda_s + 1)\, \beta \right\} - \right. \right. \\ & \chi_s \cos\left\{ (\lambda_s - 1)\, \beta \right\} \Big] + \\ & \left(\frac{\rho^*}{t_p} \right)^{\lambda_a} \mu_a \left(\lambda_a + 1 \right) \left[\sin\left\{ (\lambda_a + 1)\, \beta \right\} - \right. \\ & \chi_a \sin\left\{ (\lambda_a - 1)\, \beta \right\} \Big] + \\ & \left. C_{bw} \cdot \left\{ \left(\frac{\rho^*}{t_p} \right)^2 - \left(\frac{\rho^*}{t_p} \right) \right\} - r_s \cdot \left(\frac{\rho^*}{t_p} \right)^2 \right\} \end{aligned} \tag{3.21}$$

and in case of symmetry:

$$
\begin{aligned}
\sigma_e =& \frac{1}{\rho^*}\int_0^{\rho^*}\sigma_n(r)\mathrm{d}r \\
=& \sigma_s\cdot\left(\frac{t_p}{\rho^*}\right)\cdot\left\{\left[1-2r_s\left\{1-f\left(\frac{r}{t_p}=\frac{1}{2}\right)\right\}\right]\right. \\
& \left(\left(\frac{\rho^*}{t_p}\right)^{\lambda_s}\mu_s(\lambda_s+1)\left[\cos\left\{(\lambda_s+1)\,\beta\right\}-\right.\right. \\
& \chi_s\cos\left\{(\lambda_s-1)\,\beta\right\}\Big]+ \\
& \left(\frac{\rho^*}{t_p}\right)^{\lambda_a}\mu_a\,(\lambda_a+1)\left[\sin\left\{(\lambda_a+1)\,\beta\right\}-\right. \\
& \chi_a\sin\left\{(\lambda_a-1)\,\beta\right\}\Big]+ \\
& \left.\left.C_{bw}\cdot\left\{2\left(\frac{\rho^*}{t_p}\right)^2-\left(\frac{\rho^*}{t_p}\right)\right\}\right)+ \\
& r_s\cdot\left\{2\cdot f\left(\frac{r}{t_p}=\frac{1}{2}\right)-1\right\}\cdot \\
& \left.\left[\left\{1-f\left(\frac{r}{t_p}=\frac{1}{2}\right)\right\}\cdot\left(\frac{\rho^*}{t_p}\right)-\left(\frac{\rho^*}{t_p}\right)^2\right]\right\}.
\end{aligned}
\tag{3.22}
$$

The material characteristic length ρ^* is set to be a load level dependent parameter(Palkar,2021).

$$
\rho^* = \rho_c\left(\frac{\Delta\sigma_s/(1-r_{lr})}{\sigma_y}\right)^{\rho_p^*} \tag{3.23}
$$

where ρ_c and ρ_p^* are material fitting constants. The best fit happens at $\rho_c = 2.04$ and $\rho_p^* = 1$. σ_y is the yield strength of the material.

The effective notch stress range based on Walker's mean stress effect is calculated with:

$$
S_{e,eff} = \Delta\sigma_{e,eff} = \frac{\Delta\sigma_e}{(1-r_{lr})^{1-\gamma}} \tag{3.24}
$$

γ is found to be $\gamma = 0.67$ as the best fit. For a pure compression load case, the mean stress effect should be involved to calculate the loading & response ratio:

$$r_{rl} = \frac{\sigma_{\min} + \sigma_{res}}{\sigma_{\max} + \sigma_{\text{res}}} = \frac{r_{rl,\,\text{test}}\,\Delta\sigma + \sigma_{\text{res}}\;(1 - r_{rl,test})}{\Delta\sigma + \sigma_{\text{res}}\;(1 - r_{rl,\,\text{test}}\,)} \tag{3.25}$$

where:

$$r_{rl,\,\text{test}} = \frac{\sigma_{\min}}{\sigma_{\max}} = \frac{\sigma_{\max} - \Delta\sigma}{\sigma_{\max}} \tag{3.26}$$

When the maximum stress is zero, eq. 3.25 becomes:

$$\begin{aligned} \lim_{r_{rl,test}\to-\infty}(r_{rl}) &= \lim_{r_{rl,test}\to-\infty}\left(\frac{r_{rl,\,\text{test}}\,\Delta\sigma + \sigma_{\text{res}}\;(1 - r_{rl,\,\text{test}}\,)}{\Delta\sigma + \sigma_{res}\,(1 - r_{rl,\,\text{test}}\,)}\right) \\ &= \frac{\sigma_{\text{res}}\; - \Delta\sigma}{\sigma_{res}} \end{aligned} \tag{3.27}$$

The definition of σ_{res}, σ_{min} and σ_{max} are plotted in the figure below:

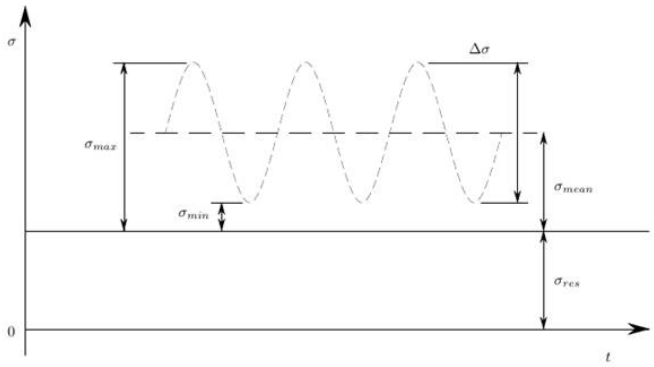

Figure 3.2: Mean stress correction for loading & response ratio

To improve the fatigue lifetime prediction accuracy, a transition curvature parameter $\rho_{S\infty}$ is introduced. Moreover, a 6-parameter $\{\log(C), m, \sigma_N, S_{\infty,\mu}, S_{\infty,\sigma}, \rho_{S_\infty}\}$ generalised random fatigue limit (GRFL) model can be obtained:

$$\log(N) = \log(C) - m \cdot \log(S) - \rho_{S_\infty} \cdot \log\left\{1 - \frac{S_\infty(\mu,\sigma)}{S}\right\} \tag{3.28}$$

For $\rho_{S\infty} \to m$ the GRFL model turns into the ordinary random fatigue limit (ORFL) one. If the data does not contain fatigue limit behaviour, the linaer Basquin (LB) model appears: $\rho_{S\infty} \to 0$.

3.3 FATIGUE DAMAGE ACCUMULATION

For variable amplitude load case, it is important on how to accumulate the damage. It can be separated into linear damage accumulation and non-linear damage accumulation. The linear damage model (LDM) is based on the hypothesis that the fatigue damage is equal to the accumulated cycle ratio:

$$D = \sum \frac{n_i}{N_i} \tag{3.29}$$

No damage is accumulated if the load is below the fatigue limit. However, linear damage model prediction shows significant discrepancies when compared with experimental data under variable amplitude load. In addition, the results are too conservative for low-to-high loading sequence fatigue while non-conservative for high-to-low loading sequence(Schütz, 1996). To overcome the disadvantages of linear damage model, non-linear accumulation models have been developed in recent years. They can be roughly divided into curve approach and continuum damage mechanics models.

3.4 CONCLUDING REMARKS

The effective notch stress is the averaged notch stress over the material characteristic length. The calculation approach of effective notch stress based total life concept are clarified in this chapter. First, far-field mechanical loading induced through-thickness weld toe notch stress calculation approach is summarized for both T-joint and cruciform joint. The obtained semi-analytical formulations of σ_e are related to the welded joint far-field stress and weld geometries. Finally, a load level dependent material characteristic length rho^* is selected

and a GRFL S-N curvce would be used to predict the lifetime of the critical hot spot.

4

LARGE SCALE SPECIMEN TOTAL LIFE ASSESSMENT

In Chapter 2, the Battelle structural stress is evaluated, and in Chapter 3, the effective notch stress-based total life estimate is presented. The constant amplitude test results of a large-scale specimen will be introduced to validate the fatigue total life estimate. As a comparison, the hot spot structural stress life time forecast based on the DNV-GL standard will also be established. To explore the influence of mesh quality, another hot spot type B Battelle structural stress will be evaluated.

4.1 STIFFENED PANEL STRUCTURAL DETAILS

This section aims to present the geometry detail, experimental detail and experimental results of the large scale specimen. Still missing the geometry description of the model.

The validation model is based on the experiments done by Polezhayeva *et al.* (2013). Fatigue tests were conducted on small specimens with longitudinal attachments and welded steel panels, representing a typical longitudinal stiffener to transverse web connection in a ship's hull. All specimens and panels were manufactured from Lloyd's Grade A steel plates with a specified minimum yield strength of 235MPa. Mechanical properties of the four thicknesses used are given in table 4.1.

Plate thickness, mm	Yield strength, MPa	Ultimate strength, MPa
6	338	471
8	347	468

Table 4.1: Mechanical properties of the specimens

Six reduced scale specimens were fatigue tested under different stress ratios. This design had six of the fillet welded joints between the buckling vertical stiffener and longitudinal flange. Fatigue failure was expected to initiate at the toes of fillet welded joints between the buckling vertical stiffener and longitudinal flange, with the fatigue crack propagating to failure through the flange thickness. The specimens were tested under axial loads, and panels were tested in three point bending to induce failure at the connection of the attachment of vertical stiffener to the longitudinal flange.

The endurance limit of the experiment is indicated by the data in table 4.2.

Table 4.2: Fatigue test results obtained from welded panels under constant amplitude loading

Panel	Limits [kN]	Range [kN]	Hot-spot stress range [MPa]	Endurance [cycles]	Failure Criterion
1	3.6 to 36	32.4	99	8300000	Run out
1A	5 to 55	50	133	1775000	Through thickness
2	8 to 80	72	196	736000	Through thickness
3	0 to -72	72	223	6773000	Through thickness
4	-36 to 36	72	200	784000	Through thickness

In some cases, sufficient strain gauges were used to enable the hot-spot stress to be determined by extrapolation. In other cases, a single gauge was attached 3.2 mm from the toe. However, it was possible to deduce the corresponding hot-spot stress on the basis that the more detailed strain measurements showed that it was reasonable to assume that the hot-spot stress was 1.16 times the stress 3.2 mm from the toe. The location of final failure and crack geometry detail can be found in table A.1.

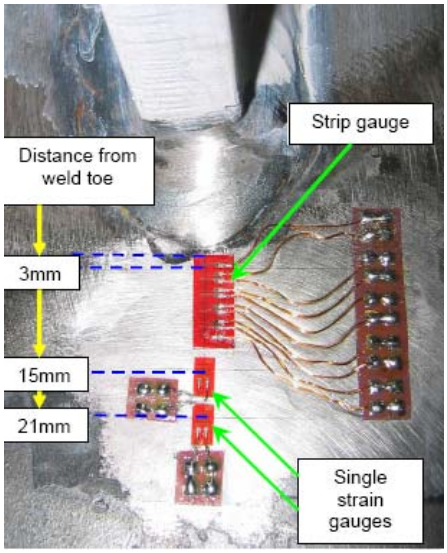

Figure 4.1: Instrumentation of welded panel: Typical strain gauge arrangement for full-scale panel

4.2 DNV-GL REFERENCE ASSESSMENT

This section aims to clarify the calculation procedure from hot spot structural stress to effective stress and total life time.

For modelling with shell elements without any weld included in the model, the hot spot stress is taken as the stress at the read out point 0.5t away from the intersection line(DNV-GL, 2016).

For modelling with three-dimensional elements with the weld included in the model, the hot spot stress is taken as the stress at the read out point 0.5t away from the weld toe. The effective hot spot stress range is derived as:

$$\sigma_{Eff} = \max \begin{cases} 1.12\sqrt{(\Delta\sigma_{\perp})^2 + 0.81\Delta\tau_{//}^2} \\ 1.12\alpha|\Delta\sigma_1| \\ 1.12\alpha|\Delta\sigma_2| \end{cases} \tag{4.1}$$

where The first principal stress is calculated as:

$$\Delta\sigma_1 = \frac{\Delta\sigma_{\perp} + \Delta\sigma_{//}}{2} + \frac{1}{2}\sqrt{(\Delta\sigma_{\perp} - \Delta\sigma_{//})^2 + 4\Delta\tau_{//}^2} \tag{4.2}$$

and

$$\Delta\sigma_2 = \frac{\Delta\sigma_{\perp} + \Delta\sigma_{//}}{2} - \frac{1}{2}\sqrt{(\Delta\sigma_{\perp} - \Delta\sigma_{//})^2 + 4\Delta\tau_{//}^2} \tag{4.3}$$

The geometry coefficient α value is defined as: $\alpha = 0.90$ if the detail is classified as C_2 with stress parallel to the weld at the hot spot in Table A-3. $\alpha = 0.80$ if the detail is classified as C1 with stress parallel to the weld at the hot spot, ref. Table A-3. $\alpha = 0.72$ if the detail is classified as C with stress parallel to the weld at the hot spot(DNV-GL, 2016).

4.3 RESULTS DISCUSSION

As mentioned in the literature(Polezhayeva *et al.*, 2013), the large scale specimen was cracked at the hot spot type A of the vertical bracket(figure 4.3) through the thickness. A FEM shell model is set up to calculate the hot spot type A structural stress, effective notch stress and finally predict the total fatigue life time.

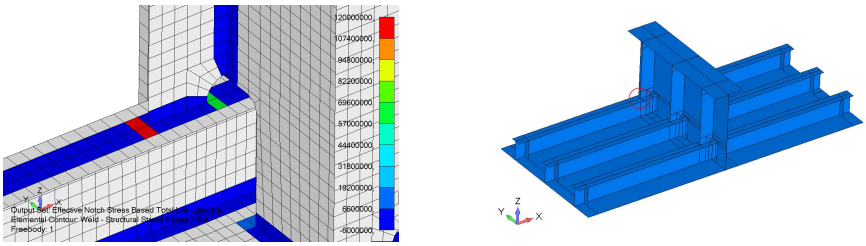

(a) Battelle structural stress range (b) Hot spot location

Figure 4.2: Validation model hot spot

In order to calculate the total life time of the large scale specimen, the Battelle structural stress and effective notch stress are necessary. Since the mesh size should be larger than $t_c/2 + l_w = 11mm$ for hot spot type A, the element size is set to be 17.5mm to perform the GVNM.

Table 4.3: 5kN to 55kN constant amplitude load results

	Load	Stress Range[MPa]	Endurance R95	Endurance R50
Experiments	5kN to 55kN	133	1775000	1775000
Hot Spot Stress	5kN to 55kN	119	812830	2818383
Effective Notch Stress	5kN to 55kN	120	742276	2336498

Table 4.4: 8kN to 80kN constant amplitude load results

	Load	Stress Range[MPa]	Endurance R95	Endurance R50
Experiments	8kN to 80kN	196	736000	736000
Hot Spot Stress	8kN to 80kN	171	212686	695599
Effective Notch Stress	8kN to 80kN	172.64	212591	846767

Table 4.5: 0kN to -72kN constant amplitude load results

	Load	Stress Range[MPa]	Endurance R95	Endurance R50
Experiments	0kN to -72kN	196	6773000	6773000
Hot Spot Stress	0kN to -72kN	171	–	–
Effective Notch Stress	0kN to -72kN	172.64	2190716	6895823

Table 4.6: 36kN to -36kN constant amplitude load results

	Load	Stress Range[MPa]	Endurance R95	Endurance R50
Experiments	35kN to -36kN	200	784000	784000
Hot Spot Stress	36kN to -36kN	172.34	212686	695599
Effective Notch Stress	36kN to -36kN	173.77	212591	856921

It can be observed that for all cases, the Battelle structural stress and hot spot structural stress range is very comparable to each

other. Based on the Battelle structural stress results and R50 S-N curve, the effective notch stress based total life estimate provides a satisfying accuracy. With the R95 S-N curve, the total life endurance limit prediction is still comparable to the hot spot structural stress prediction. In table 4.4 and 4.6, effective notch stress was giving slightly different results because of the mean stress correction, while the hot spot structural stress provided the same lifetime.

There is always tensile load remaining at the weld joint because of the weld residual stress. DNV tested many specimens and concluded that the local stress around the weld joint is still tension even for fully compression load case. Hence, they regarded fully compression as always safe. However, according to experiments done by Polezhayeva *et al.* (2013), fully compression still have damage on the structure, however, the life time is much larger than tensile load. For the total life estimate, it is still able to predict the life time for fully compression with a good matching with the experimental results.

As shown in figure 4.3a, the Battelle structural stress range is also high at the hot spot type B location, at the weld tip of the vertical bracket. Although the life time and stress results are not tested in the experiment, the effective notch stress based total life estimate can still be verified by the hot spot structural stress.

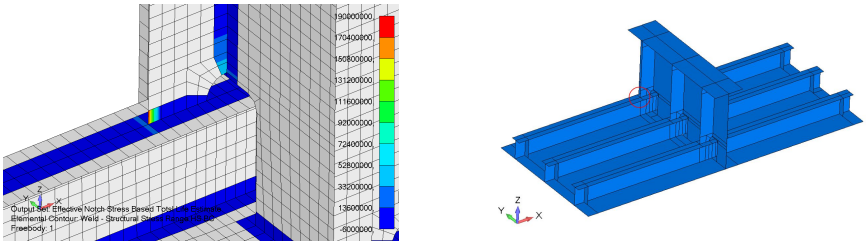

(a) Battelle structural stress range (b) Hot spot location

Figure 4.3: Validation model hot spot

According to eq.3.21 and eq. 3.22, the effective notch stress results are based on structural stress, structural stress affected ρ^* and weld geometry affected component. If the Battelle structural stress is ac-

curate, the effective notch stress will also be accurate. Therefore, the σ_s is also tested with two different mesh sizes. The weld shows in figure 4.4 appears to be the peak stress location. Hence, the visualized Battelle structural stress range and weld perpendicular stress results are plotted in that region:

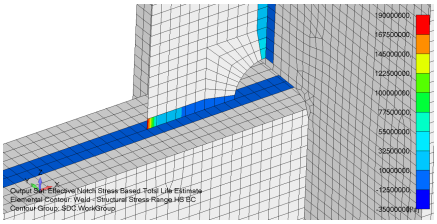

Figure 4.4: 50kN $t \times t$ Battelle

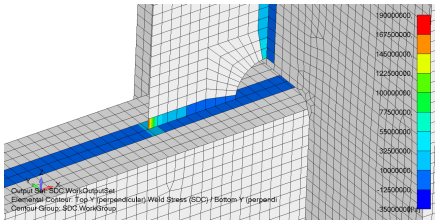

Figure 4.5: 50kN $t \times t$ elemental

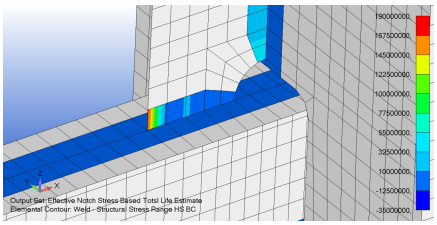

Figure 4.6: 50kN $2t \times 2t$ Battelle

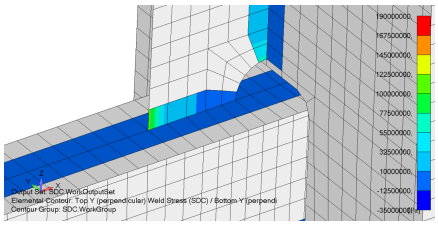

Figure 4.7: 50kN $2t \times 2t$ elemental

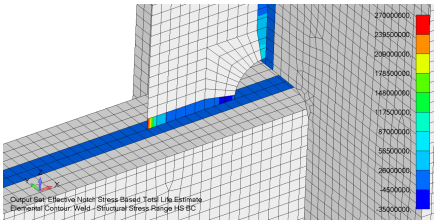

Figure 4.8: 72kN $t \times t$ Battelle

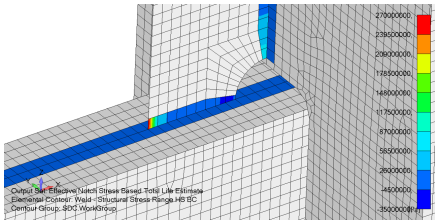

Figure 4.9: 72kN $t \times t$ elemental

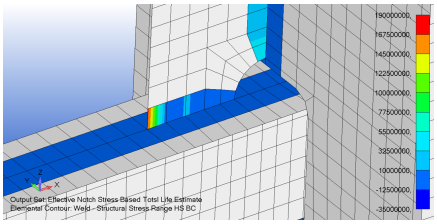

Figure 4.10: 72kN $2t \times 2t$ Battelle

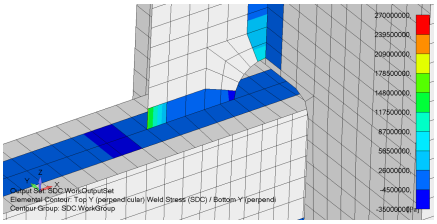

Figure 4.11: 72kN $2t \times 2t$ elemental

It can be observed that the elemental peak stress is changing significantly from $t \times t$ to $2t \times 2t$(figure 4.5 and 4.7). On the other hand, figure 4.4 and 4.6 shares a very similar peak σ_s. However, there is still some differences at the middle of the weld. Therefore, the stress along the weld is plotted in one figure to quantify the difference:

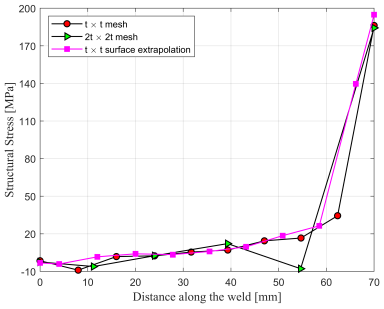

Figure 4.12: 50kN mesh convergence

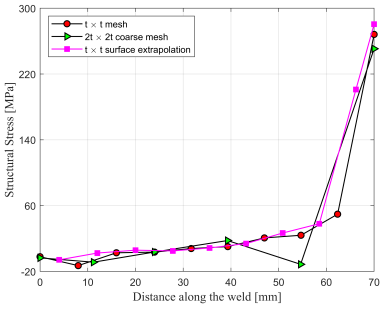

Figure 4.13: 72kN mesh convergence

From figure 4.12 and 4.13, the $t \times t$ Battelle structural stress has a very good matching with the hot spot structural stress. The $2t \times 2t$ model is matching for most of the nodes along the weld. However, the 55mm location is too low for the stress distribution line. It is because the nodal force has a very sharp increase within 1 element. The 55mm nodal results is compensating the influence of the end node and hence become lower than the hot spot structural stress.

The life time of the hot spot type B location is shown in the table below:

Table 4.7: Hot spot type B life time comparisons

	load[kN]	Endurance R95 [cycles]	Endurance R50 [cycles]
Hot spot structural stress	5 to 55	164470	539510
Effective notch stress	5 to 55	249445	785188
Hot spot structural stress	8 to 80	55081	180717
Effective notch stress	8 to 80	89921	283049
Hot spot structural stress	36 to -36	55081	180717
Effective notch stress	36 to -36	98296	309412

From table 4.7, the difference between effective structural stress and hot spot structural stress is larger than hot spot type A. Since DNV-GL is adopting the principle stress(eq.4.2), the parallel to the weld contribution and shear component is considered in some extent. For the effective notch stress based total life prediction, only mode-I crack is discussed in this project. Therefore, the difference will increase for this type B hot spot.

4.4 MESH QUALITY STUDY

In order to check the mesh quality influence on the large scale specimen, the Battelle structural stress results is also plotted on a coarse mesh model under 5 to 55kN load:

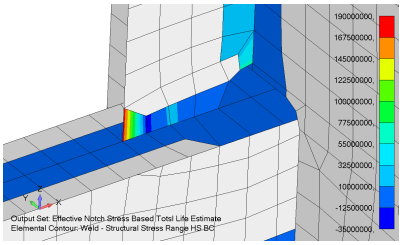

(a) 5kN to 55kN coarse mesh results

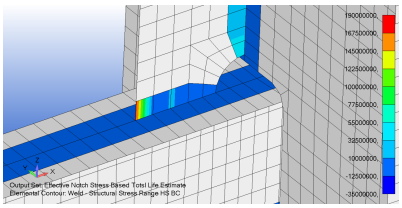

(b) 5kN to 55kN fine mesh results

Figure 4.14: Validation model hot spot

The contour plot shows a very similar Battelle stress distribution. To quantify the difference with the fine mesh model, the Battelle structural stress was plotted in one graph:

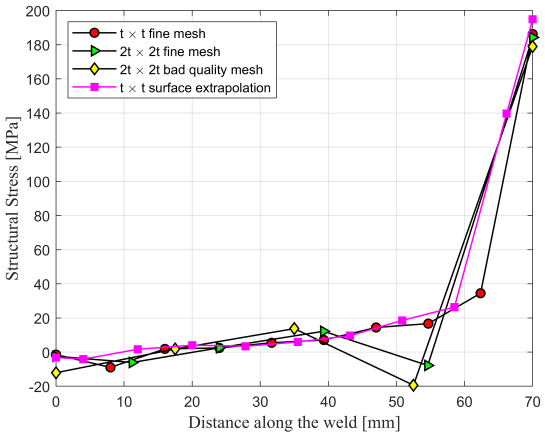

Figure 4.15: Large scale specimen mesh quality study

The peak stress of the coarse mesh model is very close to $t \times t$ and $2t \times 2t$ fine mesh. Therefore, the lifetime of the coarse mesh model will still be reliable. Because the element size is slightly larger than $2t \times 2t$, the compensation region is also extended.

4.5 CONCLUDING REMARKS

The effective notch stress based total life estimate has been used to predict the life time of a large scale specimen in this chapter. By comparing with the hot spot A experimental data and DNV-GL hot spot structural stress(DNV-GL, 2016) prediction, it can be concluded that the total life estimate of effective notch stress concept maintains good accuracy. In order to further examine the criterion, another critical crack location(hot spot B) is also verified. In this case, the life time deviation of effective notch stress based total life prediction and DNV-GL prediction trends to rise. It probably originates from the complex stress distribution at the hot spot type B location. DNV-GL considered the shear component and stress parallel to the weld contribution in some extent, but the total life evaluation for this project only accounts for mode-I crack. Finally, an ugly mesh model is created to evaluate the influence of mesh quality. The peak stress continues to converge for both the good mesh and poor mesh models, indicating that the later total life projection is accurate. However, the compensation effect is more pronounced in the ugly mesh model than its fine mesh counterpart. This is due to the growing mesh size of the ugly element.

5

EVALUATION

In this chapter, the solutions to the research questions are stated and the research's conclusions are presented. Several outcomes will then be briefly addressed, followed by a review of the previously indicated recommendations.

5.1 DISCUSSIONS

In general, the effective notch stress-based total life estimate accurately predicts the lifetime of structures subject to mode-I crack. The comparison between the large-scale specimen test findings and the small-scale specimen test results demonstrates satisfactory accuracy. However, Battelle structural stress has some limitations that may affect the accuracy of total life prediction.

Hot Spot Type A

First of all, the generalized virtual node method for hot spot type A calculation requires the element size to be larger than $t_c/2 + t_w$. Therefore, a value equal or larger than $2t \times 2t$ is recommended for meshing a model. In addition, there should be at least two element in between of the edge and hot spot location to capture the bending component, which indicates the element size cannot go beyond half the plate width. By comparing the results of different ugly ele-

ment examples, the center edge of the elements at the weld end is recommended to always align with the weld extension line.

Hot Spot Type B and C

The first thing should be highlighted is that there must be at least 4 elements along the weld to capture the structural stress accurately (hot spot B and C). For hot spot type B, generalized virtual node method should be applied to redistribute the stress near the weld tip location. The l_1 linearization can be adopted on element size smaller than $t \times t$ to smooth the stress distribution line. For hot spot type C, the generalized virtual node method can also be applied to obtain a slightly more converged value at the end of the weld.

Compensation Effect

When the sharp increase is happening at the end of a weld, the compensation effect would not affect the peak structural stress results(figure 4.12 and 4.13) due to the application of generalized virtual node method. However, it will still have impact on the adjacent area and result in spiky behavior for mesh sizes above a specific threshold. More research can be conducted on this issue in the future.

5.2 CONCLUSIONS

In this thesis, at first all the input parameters are collected from a FEM model. The Battelle structural stress model is implemented to capture the through-thickness linearized stress values. In this stage, three specimens are used to verify the stress value for the three types of hot spot. Mesh quality study is conducted and quantified with Jocobian and internal angles. Separated weld influence is also presented with different element sizes. Then the effective notch stress based total life estimate is clarified and validated by a large scale specimen test results. Four constant amplitude load cases are modeled and the critical hot spot type A life time prediction is compared with the test record. For all load cases, the effective notch stress shows satisfactory accuracy. Moreover, the hot spot type B structural stress results are

also measured in order to verify the total life estimate. By comparing the coarse mesh and fine mesh results, it can be concluded that the total life estimate is also able to proceed the calculation even for coarse mesh.

5.3 RECOMMENDATIONS

Based on section 5.1, some further study can be formed to improve the project results. First of all, it is possible to ameliorate the weld recognition. As shown in figure 4.14b, the hot spot is not recognized as Type A because it is also part of hot spot type C on the joint of stiffener flange and web. It could be captured as both hot spot type C and A to present all possible hot spot. Secondly, the effective notch stress results is sensitive to the weld dimensions. In this project, $l_w = h_w = t_p$ is assumed for convenience. This geometry parameter can be quantified in the future to improve the lifetime accuracy.

At the validation stage, only constant amplitude load data for large-scale specimens are compared. The results of variable amplitude loading can also be evaluated using the state-of-the-art damage accumulation model. In addition, the compression load case of curved weld can be finalized in the later stage. In this project, the key parameter that could determine the positive perpendicular to the weld direction is missing. Geometry input such as element center coordinates should help determine the local abscissa and compression load case could be estimated accurately. Finally, the method is only able to predict the life time for mode-I crack. Researchers in the future can adopt multi-axial load criterion to better determine the lifetime of complicated structure, such as the hot spot B prediction in figure 4.3b.

This page intentionally left blank

A

EXPERIMENTAL DETAIL

Panel 1A: Constant Amplitude, $R = 0.1, 50\text{kN}$ load range

This panel was tested with a fully tensile load range of 50kN and a stress ratio 0.1. A 2 mm long crack was first detected after 75,000 cycles at weld toe W1B, but it did not propagate further during the test. At Weld W3A, a 5 mm crack was detected on the surface after 175,000 cycles, which propagated through-thickness cracking after $1,775,000$ cycles. With a final surface crack length of 31 mm, the aspect ratio of the crack at final failure was therefore around 4.

Panel 2: Constant Amplitude, $R = 0.1, 72\text{kN}$ load range

Panel 2 was tested under a fully tensile load cycling between 8 and 80kN, which resulted in a load range of 72kN and a stress ratio $R = 0.1$. An ACPD unit was used to measure the crack depth. First fatigue cracking was simultaneously detected at the top and bottom weld toes (ie that on the flange and that on the stiffener) in Welds W1A, W2A, W3A after 292,000 fatigue cycles. These cracks were removed using a pencil grinder and then repaired following the repair procedure. Further cracking occurred at Welds W1A and W3A and both cracks propagated to through-thickness after 736,000 cycles had been applied. No cracking was detected at Weld W1B. At weld W2B, a fatigue crack was detected at the upper toe after 361,000 cycles. After removing the crack and repairing the weld, the test was continued. Another crack was detected at the same weld after 433,000 cycles and propagated until the test stopped. At Weld W3B,

a fatigue crack was detected after 331,000 cycles and propagated without repair until the test was stopped. The order of appearance of fatigue cracks in Panel 2 can be seen from Table 9.1

Panel 3: Constant amplitude, zero-compression, 72kN load range

Panel 3 was tested under fully compressive loading between 0 and 72kN, resulting in a range of 72kN. First cracking of 2 mm surface length was detected at weld W3B after 4,748,000 cycles. Through-thickness cracking occurred at weld W3A after 6,773,000 cycles, with a surface crack length of 27.5 mm.

Panel 4: Constant Amplitude, $R = -1$, 72kN load range

In Panel 4 the applied loading alternated between −36kN and +36kN; giving a load range of 72kN and a stress ratio of -1. ACPD was used to monitor crack growth through the thickness. First cracking was simultaneously detected after 171,000 cycles at weld toes W2A (10mm long crack), W3A (3mm long crack), W2B (9mm long crack) and W3B (2mm long crack). Repair was not attempted and cracks were monitored until through-thickness at weld toes W2A and W2B after 784,000 cycles when the test was stopped. At the end of the test, the depth of the crack measured using a probe was 1.2 mm at weld W1A, 2.3 mm at W3 A and 2 mm at W3B. No crack was observed at weld toe W1B. The order of appearance of fatigue cracks in Panel 4 can be seen from Table 9.2. Before testing, the stress range measured at 3.2 mm from the weld toes was between 155 and 175MPa for the six joints but decreased during the fatigue test as cracks developed at the weld toes.

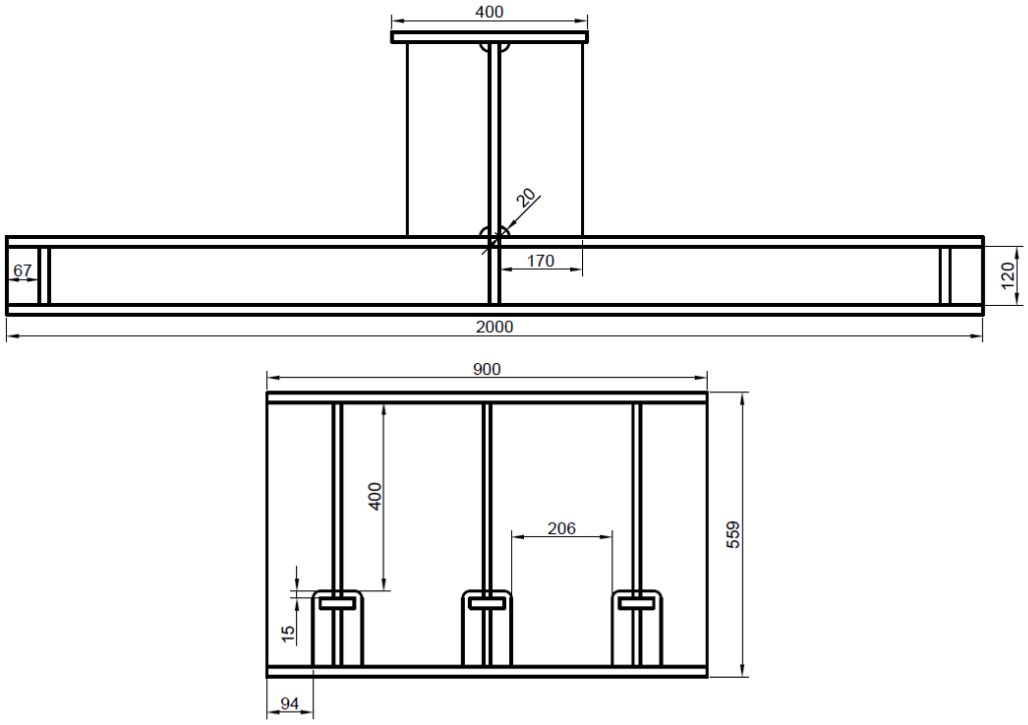

Figure A.1: Dimensions of the large scale specimen

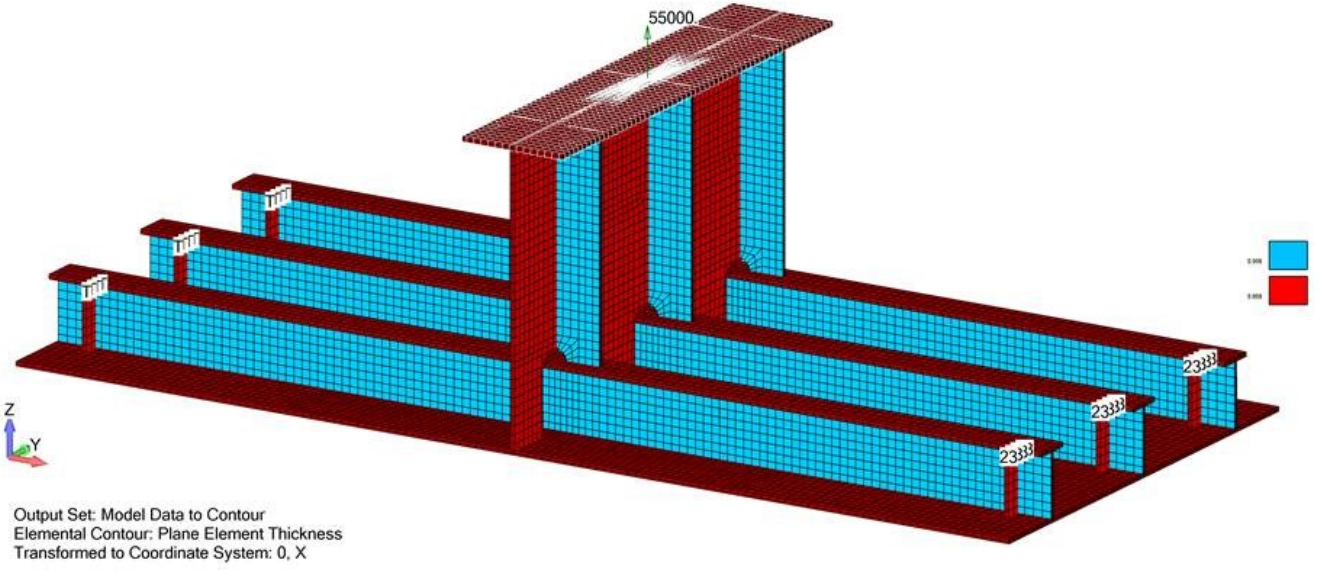

Figure A.2: Plate thickness of the large scale specimen

Specimens	Stress Ratio	Hot-spot stress range (linear), [MPa]	Weld	Cycles at first crack detection	Fatigue life at first crack detection,%	Surface crack length at first detection, mm	Final Length surface crack mm	Cycles at test stop	Remarks
Panel 1 32.4 kN load range Constant Amplitude	0.1	76.8	W1A					83000000	No crack at weld toe - run out
		88.7	W2A						
		69.6	W3A						
		85.8	W1B						
		80.9	W2B						
		99.4	W3B						
Panel 1A 50kN load range Constant Amplitude	0.1	CrackFirst	W1A	325000	18	2	13	1775000	
			W2A	400000	23	2	16		
		CrackFirst	W3A	175000	10	5	31		Through thickness
			W1B	75000	4	2	2		No crack propagation
		128.8	W2B	900000	51	6	6		No crack propagation
		136.5	W3B	875000	49	6	11		
Panel 2 72kN load range Constant Amplitude	0.1	205.2	W1A	292000	40		30	736000	Through thickness
		197.1	W2A	292000	40		24		
		187.2	W3A	292000	40		29		Through thickness
		185.4	W1B						No crack
		207	W2B	433000	59	8	14		
		216.9	W3B	311000	45	7	7		

Table A.1: Summary of fatigue test conditions and results for all welded panels.

Specimens	Stress Ratio	Hot-spot stress range (linear), [MPa]	Weld	Cycles at first crack detection	Fatigue life at first crack detection,%	Surface crack length at first detection, mm	Final Length surface crack mm	Cycles at test stop	Remarks
Panel 3 72kN load range Constant Amplitude	Zero-compression		W1A	5223000	77	2	4	6773000	No crack propagation
			W2A	5423000	80	2	2		No crack propagation
			W3A	4848000	72	0.5	27.5		Through thickness
			W1B						No crack
			W2B	5248000	77	2	4		No crack propagation
			W3B	4748000	70	2	2		No crack propagation
Panel 4 72kN load range Constant Amplitude	-1	CrackFirst	W1A	245000				784000	Through thickness
			W2A	171000					Through thickness
			W3A	171000					
			W1B						No crack
			W2B	171000					Through thickness
			W3B	171000					

Table A.2: Summary of fatigue test conditions and results for all welded panels.

BIBLIOGRAPHY

Alencar, G., de Jesus, A., da Silva, J. G. S., & Calçada, R. (2021). A finite element post-processor for fatigue assessment of welded structures based on the master s-n curve method. *International Journal of Fatigue*, *153*, 106482. https://doi.org/https://doi.org/10.1016/j.ijfatigue.2021.106482

Darcis, P. P., Lassen, T., & Récho, N. (2006). Fatigue behavior of welded joints part 2: Physical modeling of the fatigue process. *Welding Journal*, *85*.

den Besten, H. (2018). Fatigue damage criteria classification, modelling developments and trends for welded joints in marine structures. *Ships and Offshore Structures*, *13*(8), 787–808. https://doi.org/10.1080/17445302.2018.1463609

den Besten, J. H. (2015). *Fatigue resistance of welded joints in aluminium high-speed craft: A TOTAL STRESS CONCEPT* (Doctoral dissertation). https://doi.org/10.4233/uuid:370b3d44-f4a6-403e-9629-d36174c3aca4

DNV-GL. (2016). DNVGL-RP-c203: Fatigue design of offshore steel structures. *DNV GL - Recommended Practice*.

Dong, P. (2005). A Robust Structural Stress Method for Fatigue Analysis of Offshore/Marine Structures. *Journal of Offshore Mechanics and Arctic Engineering*, *127*(1), 68–74. https://doi.org/10.1115/1.1854698

Glinka, G., & Shen, G. (1991). Universal features of weight functions for cracks in mode i. *Engineering Fracture Mechanics*, *40*(6), 1135–1146. https://doi.org/https://doi.org/10.1016/0013-7944(91)90177-3

Kim, M. H., Kang, S. W., Kim, J. H., Kim, K. S., Kang, J. K., & Heo, J. H. (2010). An experimental study on the fatigue strength assessment of longi-web connections in ship structures using structural stress. *International Journal of Fatigue*, *32*(2), 318–329. https://doi.org/https://doi.org/10.1016/j.ijfatigue.2009.06.018

Lee, J.-M., Seo, J.-K., Kim, M.-H., Shin, S.-B., Han, M.-S., Park, J.-S., & Mahendran, M. (2010). Comparison of hot spot stress evaluation methods for welded structures. *International Journal of Naval Architecture and Ocean Engineering*, *2*(4), 200–210. https://doi.org/https://doi.org/10.2478/IJNAOE-2013-0037

Neuber, H. (1961). Theory of Stress Concentration for Shear-Strained Prismatical Bodies With Arbitrary Nonlinear Stress-Strain Law. *Journal of Applied Mechanics*, *28*(4), 544–550. https://doi.org/10.1115/1.3641780

Noroozi, A., Glinka, G., & Lambert, S. (2005). A two parameter driving force for fatigue crack growth analysis [Fatigue Damage of Structural Materials V]. *International Journal of Fatigue*, *27*(10), 1277–1296. https://doi.org/10.1016/j.ijfatigue.2005.07.002

Paris, P. C. (2014). A brief history of the crack tip stress intensity factor and its application. *Meccanica*, *49*(7), 759–764. https://doi.org/10.1007/s11012-014-9896-y

Polezhayeva, H., Maddox, S. J., Howarth, D., & Robinson, A. (2013). *Fatigue Testing to Identify Effect of Mean Stress on Fatigue Strength of Welded Joints in Ship Structures* (Vol. All Days) [ISOPE-I-13-631].

Sadananda, K., & Vasudevan, A. (2003). Fatigue crack growth mechanisms in steels [International Conference on Fatigue Damage of Structural Materials IV]. *International Journal of Fatigue*, *25*(9), 899–914. https://doi.org/https://doi.org/10.1016/S0142-1123(03)00128-2

Schütz, W. (1996). A history of fatigue. *Engineering Fracture Mechanics*, *54*(2), 263–300. https://doi.org/10.1016/0013-7944(95)00178-6

Susmel, L., & Taylor, D. (2007). A novel formulation of the theory of critical distances to estimate lifetime of notched components in the medium-cycle fatigue regime. *Fatigue & Fracture of Engineering Materials & Structures*, *30*, 567–581. https://doi.org/10.1111/j.1460-2695.2007.01122.x

Taylor, D. (1999). Geometrical effects in fatigue: A unifying theoretical model. *International Journal of Fatigue*, *21*(5), 413–420. https://doi.org/10.1016/S0142-1123(99)00007-9

Yang, X., Wang, J., & Liu, J. (2011). High temperature LCF life prediction of notched DS ni-based superalloy using critical distance concept. *International Journal of Fatigue*, *33*(11), 1470–1476. https://doi.org/10.1016/j.ijfatigue.2011.05.018

This page intentionally left blank

COLOPHON

This document was typeset using the typographical look-and-feel `classicthesis` developed by André Miede and Ivo Pletikosić. The style was inspired by Robert Bringhurst's seminal book on typography *"The Elements of Typographic Style"*. `classicthesis` is available for both LaTeX and LyX:

https://bitbucket.org/amiede/classicthesis/

Happy users of `classicthesis` usually send a real postcard to the author, a collection of postcards received so far is featured here:

http://postcards.miede.de/

Thank you very much for your feedback and contribution.

Final Version as of November 23, 2022 (classicthesis v4.6).